Enhanced methane monitoring: A globally harmonized daily 0.1° XCH_4 through machine learning-based fusion of GOSAT, GOSAT-2, and TROPOMI

Jebun Naher Keya[1,★], Yejin Kim[1,★], Hyunyoung Choi[1], Jungho Im[1,2,3,*]

[1]Department of Civil, Urban, Earth, & Environmental Engineering, Ulsan National Institute of Science and Technology, Ulsan, 44919, Republic of Korea
[2]Graduate School of Carbon Neutrality, Ulsan National Institute of Science and Technology, Ulsan, 44919, Republic of Korea
[3]Artificial Intelligence Graduate School, Ulsan National Institute of Science and Technology, Ulsan, 44919, Republic of Korea

*Corresponding Author: Jungho Im (ersgis@unist.ac.kr)

★These authors contributed equally to this work.

Abstract. Accurate global monitoring of atmospheric methane (CH_4) is essential for tracking progress toward climate mitigation targets such as the Global Methane Pledge (GMP). Ground-based measurement networks are too sparse to provide sufficient spatial coverage, while satellite-derived retrievals are hindered by systematic biases and uncertainties, limiting their reliability for consistent global monitoring. We present the first global fusion of GOSAT, GOSAT-2, and TROPOMI to generate a globally consistent daily 0.1° land dataset for 2020–2023 for enhanced global column-averaged dry-air mole fraction of atmospheric methane (XCH_4) mapping. The framework employs a three-step machine-learning (ML) approach: (1) sensor-specific bias correction using TCCON observations, (2) cross-sensor harmonization to GOSAT-2, the sensor with the strongest post-correction TCCON agreement, and (3) priority-based fusion. Tree-based ensemble regressors were trained with satellite retrieval parameters to reduce systematic biases and inter-sensor discrepancies. Independent validation at three withheld TCCON stations demonstrates robust generalization of the fused product (R^2 = 0.81, RMSE = 10.78 ppb), outperforming standard and operational bias-corrected satellite products and previously reported ML-based approaches. Regional assessments show that fusion substantially improves data availability and reduces systematic errors, delivering up to 12% relative coverage gains and 33–94% bias reductions compared to TROPOMI operational products in challenging regions (South Asia, Amazon Basin, Eastern Siberia).The fused dataset reveals intensifying positive XCH_4 anomalies (+60 ppb) over South Asia, East Asia, and Central Africa during 2020–2023, linked to MODIS-derived agricultural and urban land classes as well as known oil and gas fields. The dataset provides a scalable resource for regional CH_4 emissions assessment and continuous monitoring, with the framework extendable to upcoming satellite missions (GOSAT-GW, CO2M) for long-term GMP progress tracking.

1 Introduction

Methane (CH_4) is a potent greenhouse gas (GHG), contributing approximately 0.6 °C of global warming since the pre-industrial era and accounting for nearly 30% of the observed increase in global mean surface temperature (Naik et al., 2021; IEA, 2025). Despite lower atmospheric concentrations than CO_2, its global warming potential is 28 times higher over a 100-year horizon (Myhre et al., 2013; IPCC, 2014). Its high radiative efficiency, combined with a relatively short atmospheric lifetime due to oxidation by hydroxyl radicals (OH), makes CH_4 an especially effective target for near-term climate mitigation (Prather et al., 2012; Nisbet et al., 2020). Recent observations show that CH_4 levels have been rising at an unprecedented rate, with 2020–2022 marking the fastest growth since systematic monitoring began (Saunois et al., 2025). Major CH_4 sources include anthropogenic activities (livestock farming, rice cultivation, fossil-fuel exploitation, and waste management) and natural wetland emissions (Saunois et al., 2025). Reflecting the urgency of mitigation, the Global Methane Pledge (GMP), launched at the 26th Conference of the Parties (COP26), aims to reduce global CH_4 emissions by at least 30% from 2020 levels by 2030 (IEA, 2022). Accurate quantification of the column-averaged dry-air mole fraction of atmospheric methane (XCH_4) is therefore essential for identifying emission sources and evaluating progress toward climate goals.

Ground-based monitoring systems such as the Total Carbon Column Observing Network (TCCON) provide high-precision XCH_4 measurements and serve as key reference data for satellite validation and bias correction. Despite their accuracy, TCCON sites are limited in number and spatially sparse (Lorente et al., 2021), leaving large observational gaps across Africa, South America, and large parts of Asia. Satellite platforms help address these limitations by providing broad spatial coverage. The GHGs Observing Satellite (GOSAT), GOSAT-2, and the TROPOspheric Monitoring Instrument (TROPOMI) have enabled global-scale mapping of XCH_4 and have been widely used for emission estimation and inverse modeling (Qu et al., 2021; Worden et al., 2022; Nesser et al., 2024; Maasakkers et al., 2019; Janardanan et al., 2020). However, these instruments exhibit distinct trade-offs in spatial resolution, revisit frequency, and retrieval accuracy. GOSAT and GOSAT-2 provide high spectral resolution (0.2 cm^{-1}) but limited spatial and temporal coverage with ∼10 km circular footprints and multi-day revisit intervals (Kuze et al., 2016; Suto et al., 2021). In contrast, TROPOMI offers near-daily global coverage at finer spatial resolution (5.5×7 km^2) but suffers from larger retrieval uncertainties due to lower spectral sensitivity and greater vulnerability to clouds and aerosols (Jacob et al., 2022; Hasekamp et al., 2021; Umezawa et al., 2025). As a result, no single satellite can offer both the accuracy and coverage desirable for robust global-scale XCH_4 monitoring, making multi-sensor data fusion necessary. However, merging multiple sources first requires addressing the systematic biases inherent to each sensor to ensure inter-sensor consistency.

Previous bias correction studies have relied on statistical regression approaches that account for factors such as surface albedo, aerosol loading, and viewing geometry (Inoue et al., 2016), as well as small-area approximation methods that derive surface albedo–related biases directly from satellite observations (Lorente et al., 2021). However, such methods can struggle to capture nonlinear, sensor-specific bias structures. Machine learning (ML) approaches, including Random Forest (RF), Light Gradient Boosting Machine (LightGBM), and eXtreme Gradient Boosting (XGBoost), have demonstrated improved bias correction performance by learning complex relationships between retrieval errors and environmental or observational predictors (Balasus et al., 2023; Schneising et al., 2022; Li et al., 2024).

Despite these advances, several limitations remain. Some studies improve spatial coverage but retain substantial residual bias (Li et al., 2024), whereas others reduce systematic bias by applying global offsets to match TCCON means (Balasus et al., 2023; Parker et al., 2020), an approach that can ignore regional variations in sensor bias. Moreover, most prior work has focused on single-sensor enhancement or limited dual-sensor combinations (e.g., GOSAT + TROPOMI), leaving the potential of multi-sensor fusion underexplored (Fan et al., 2024; Balasus et al., 2023; Li et al., 2024). In contrast, XCO_2 research has increasingly adopted multi-platform fusion (e.g., OCO-2, OCO-3, GOSAT, and GOSAT-2) as a standard approach (Chen et al., 2024; Wang et al., 2022), while comprehensive global XCH_4 fusion products remain comparatively scarce. To the best of our knowledge, GOSAT-2 has not yet been incorporated into a global XCH_4 fusion product, despite its improved spectral performance and expanded coverage relative to GOSAT.

To address these gaps and enable consistent global XCH_4 monitoring, we develop an ML-based multi-sensor harmonization and fusion framework that (1) corrects sensor-specific biases using TCCON observations, (2) harmonizes all satellite retrievals to the most accurate sensor (GOSAT-2), and (3) fuses the harmonized retrievals to maximize daily spatial coverage while preserving accuracy. The resulting product provides global daily XCH_4 over land (60°S–80°N) at 0.1° resolution for 2020–2023, with improved accuracy and spatiotemporal coverage, compared to individual sensor retrievals. This enhanced dataset enables more reliable regional emission analysis, hotspot identification, and source characterization.

2 Datasets

2.1 Ground XCH$_4$ observations

TCCON is a global network of ground-based Fourier transform spectrometers (FTSs) that record direct solar spectra in the near-infrared (NIR) region (Wunch et al., 2011). TCCON serves as a benchmark dataset for validating satellite-derived XCH$_4$ because its measurements are minimally affected by aerosol loading, airmass uncertainty, and surface-reflectance variability compared with SWIR satellite retrievals (Dils et al., 2014; Malina et al., 2022). We obtained latest TCCON GGG2020 dataset from the TCCON data archive hosted by CaltechDATA (https://tccondata.org/, last accessed 26 December 2025) spanning January 2020 to December 2023, covering the overlapping observation period of TROPOMI, GOSAT, and GOSAT-2. Stations used in this study are shown in Fig. 1 and listed in Table 1.

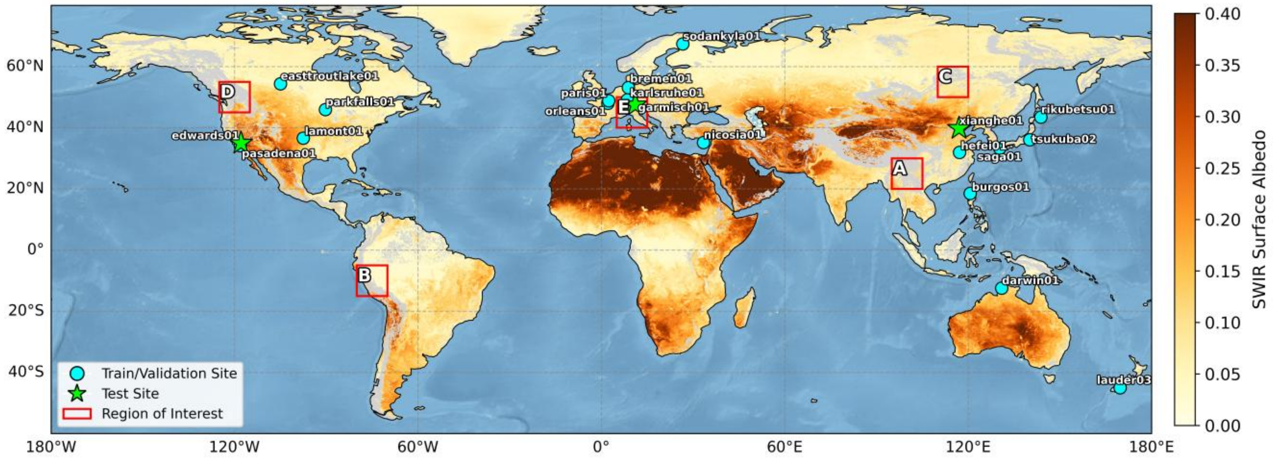

Figure 1. Study domain and TCCON stations (GGG2020 XCH$_4$) used during 2020–2023. Cyan circles denote stations used for model training/validation. Green stars indicate independent test stations held out from training and used only for evaluation of the fused XCH$_4$ product. Black boxes (A–E) denote regions of interest used for regional analyses in Section 4.3. The background map shows the 2020–2023 mean SWIR surface albedo from TROPOMI.

Table 1. TCCON (GGG2020 version) sites used for evaluation of satellite XCH$_4$ and machine learning based bias correction.

TCCON site	Latitude, Longitude (°)	Elevation (m)	Data reference
Bremen[a, b]	53.10, 8.85	30	Notholt et al., 2022
Burgos	18.53, 120.65	35	Morino et al., 2022a
Darwin	12.46, 130.93	37	Deutscher et al., 2023
East Trout Lake	54.35, -104.99	501.8	Wunch et al., 2022
Edwards[c]	34.96, -117.88	888	Iraci et al., 2022
Garmisch[c]	47.48, 11.06	743	Sussmann et al., 2025
Hefei	31.90, 117.17	30	Liu et al., 2023
Karlsruhe	49.10, 8.44	119	Hase et al., 2024
Lamont	36.60, -97.49	320	Wennberg et al., 2025
Lauder	-45.04, 169.68	370	Pollard et al., 2022
Nicosia[a]	35.14, 33.38	185	Petri et al., 2024
Orléans	47.97, 2.11	130	Warneke et al., 2024
Paris	48.85, 2.36	60	Té et al., 2022
Park Falls	45.95, -90.27	442	Wennberg et al., 2022a
Pasadena	34.14, -118.13	210	Wennberg et al., 2022b
Rikubetsu[a]	43.46, 143.77	380	Morino et al., 2022b
Saga	33.24, 130.29	7	Shiomi et al., 2022
Sodankylä	67.37, 26.63	188	Kivi et al., 2022
Tsukuba	36.05, 140.12	31	Morino et al., 2022c
Xianghe[c]	39.75, 116.96	36	Zhou et al., 2022

[a] Sites excluded from the GOSAT evaluation under the GOSAT colocation criteria. [b] Sites excluded from the GOSAT-2 evaluation under the GOSAT-2 colocation criteria. [c] Independent test sites not used for training/validation of the machine learning based bias-correction model.

2.2. Satellite XCH_4 products

This study used XCH_4 products from TROPOMI, GOSAT, and GOSAT-2. These satellite platforms have been widely used for regional and global greenhouse gas monitoring, emission estimation, and multi-sensor XCH_4 data integration (Balasus et al., 2023; Fan et al., 2024; Bao et al., 2025; Wang et al., 2025; Liu et al., 2026; Lee et al., 2025: Choi et al., 2026). All three missions retrieve XCH_4 using full-physics algorithms that simultaneously estimate surface albedo, atmospheric scattering, and trace-gas concentrations from SWIR and NIR spectra (Butz et al., 2011). However, full-physics retrievals are sensitive to clouds, aerosols, and surface heterogeneity, increasing retrieval bias and reducing data availability in high-aerosol regions and complex terrain (Jacob et al., 2022; Umezawa et al., 2025). GOSAT and GOSAT-2 provide high-precision measurements with spectral resolution approximately four times finer than that of TROPOMI (Kuze et al., 2009; Kuze et al., 2016; Suto et al., 2021; Jacob et al., 2022; Noël et al., 2021; Table 2), whereas TROPOMI offers daily global mapping, which increases data density despite higher susceptibility to atmospheric interference (Hu et al., 2018; Qu et al.,2021).These contrasting characteristics reflect an inherent trade-off between sampling density and retrieval accuracy. Table 2 summarizes mission specifications, and Fig. 2 illustrates daily sampling patterns

Table 2. Key specifications of GOSAT, GOSAT-2, and Sentinel-5P/TROPOMI XCH_4 products used in this study.

	GOSAT	GOSAT-2	TROPOMI
Local overpass time	13:00	13:00	13:30
Pixel size	10.5 km diameter	9.7 km diameter	5.5×7 km^2
Pixel separation	260–280 km	260–280 km	None
Coverage	global	global	global
Revisit time	3 days	6 days	Sub-daily
Spectral resolution	0.06 nm	0.06 nm	0.25 nm
Retrieval type	full physics	full physics	full physics
Retrieval version	v03.05	v02.00	version 02.04.00
Number of retrievals per day (pixel)[a]	360	908	386,233

[a] The number of XCH_4 retrievals per day represents the average soundings calculated per day over the full study period from 1 January 2020 to 31 December 2023.

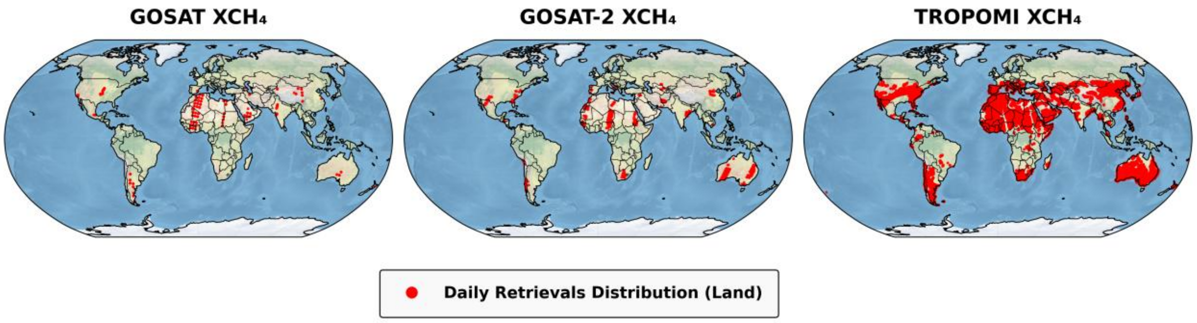

Figure 2. Spatial distribution of daily XCH_4 retrievals over land on 1 January 2020 from GOSAT, GOSAT-2, and TROPOMI. Red markers indicate native pixel locations of individual soundings and are enlarged for visualization purposes.

2.2.1. GOSAT

GOSAT (also known as *Ibuki*), launched in 2009, carries the Thermal and NIR Sensor for carbon Observation Fourier transform spectrometer (TANSO-FTS) and the TANSO Cloud and Aerosol Imager (CAI) in a sun-synchronous orbit at 666 km (Kuze et al., 2009). TANSO-FTS measures high-resolution spectra in the SWIR and thermal infrared bands, which are used to retrieve column abundances of CO_2 and CH_4 (Yoshida et al., 2011). We used the NIES SWIR L2 CH_4 product (v03.05) from GOSAT Data Archive Service (GDAS: https://data2.gosat.nies.go.jp/, last accessed 26 December 2025), which provides both bias-uncorrected (hereafter standard) and bias-corrected retrievals calibrated against TCCON GGG2014 (Inoue et al., 2016). The standard product was used as ML model input, while the bias-corrected product was used for comparison.

2.2.2 GOSAT-2

GOSAT-2, the successor of GOSAT was launched in 2018, carries upgraded TANSO-FTS-2 and CAI-2 with an intelligent cloud-avoidance pointing strategy, enabling enhanced sensitivity and expanded spatial coverage (Suto et al., 2021; Imasu et al., 2023; Park et al., 2024). GOSAT-2 extends Band 3 spectral coverage to 2.33 µm (compared to 2.08 µm for GOSAT), capturing additional CH_4 absorption features. We used the SWIR Level-2 full-physics XCH4 product (v02.00; hereafter standard) from the GOSAT-2 archive (https://data2.gosat.nies.go.jp/, last accessed 26 December 2025). To ensure high data reliability, only retrievals with quality flag = 0 were retained for bias-correction modeling.

2.2.3 TROPOMI

TROPOMI, the sole payload on ESA's Sentinel-5 Precursor (S5P) mission launched in 2017, is a nadir-viewing push-broom hyperspectral imaging spectrometer that measures radiance from the ultraviolet (UV) to the SWIR (Veefkind et al., 2012). CH_4 retrievals are derived using the RemoTeC algorithm (Hasekamp et al., 2021), and the sun-synchronous orbit with an approximately 2,600 km swath width enables near-daily global mapping of atmospheric CH_4. We used the S5P Level-2 XCH_4 product (S5P_L2__CH4____HiR) from NASA Goddard Earth Sciences Data and Information Services Center (GES DISC; https://doi.org/10.5270/S5P-3lcdqiv, last accessed 26 December 2025). This dataset provides both uncorrected XCH_4 (hereafter standard) and the posteriori albedo-dependent bias corrected XCH_4 (Lorente et al., 2021), along with associated retrieval parameters. For consistency with GOSAT and GOSAT-2, we selected standard XCH_4 retrievals with a quality assurance flag qa_value = 1 as model input, while the official bias-corrected product was used for comparison.

3 Methodology

To address limitations of single-sensor CH_4 retrievals and inter-satellite inconsistencies, we developed an integrated ML framework that combines bias correction, cross-sensor harmonization, and multi-sensor fusion of XCH_4 retrievals from TROPOMI, GOSAT, and GOSAT-2. The framework produces a globally harmonized daily 0.1° land XCH_4 product for 2020–2023 through three hierarchical steps (Fig. 3):

Step 1: Sensor-specific bias correction using TCCON as the calibration standard.

Step 2: Inter-satellite harmonization by aligning all datasets to the most accurate sensor (bias-corrected GOSAT-2).

Step 3: Multi-sensor fusion to maximize daily spatial coverage while preserving accuracy.

We define the systematic retrieval bias for a given satellite observation as:

$$\Delta_{\mathrm{Bias}} = XCH_{4,Satellite} - XCH_{4,Reference} \qquad (1)$$

where $XCH_{4,Satellite}$ denotes the standard (uncorrected) satellite retrieval and $XCH_{4,Reference}$ denotes the reference value (TCCON in Step 1; bias-corrected GOSAT-2 in Step 2). For BC, we used ensemble tree-based regressors (RF and XGBoost) due to their strong performance and stability in tabular regression with nonlinear interactions (Hwang et al., 2023; Shwartz-Ziv and Armon, 2022). For GOSAT and GOSAT-2, the predictor set additionally included co-retrieved XCO_2-related variables because CH_4 and CO_2 are retrieved simultaneously from the same SWIR spectra using a shared full-physics forward model (Butz et al., 2010). Scattering-induced light-path errors often affect both gases in a correlated manner (Oshio et al., 2020). As TROPOMI does not retrieve CO_2, only XCH_4 retrieval parameters were selected based on established practice (Balasus et al., 2023). Using these parameters, mission-specific BC models were trained to predict bias ($\hat{\Delta}_{Bias}$) and the predicted bias was subtracted from the original retrieval:

$$XCH_{4,BC} = XCH_{4,Satellite} - \hat{\Delta}_{Bias} \qquad (2)$$

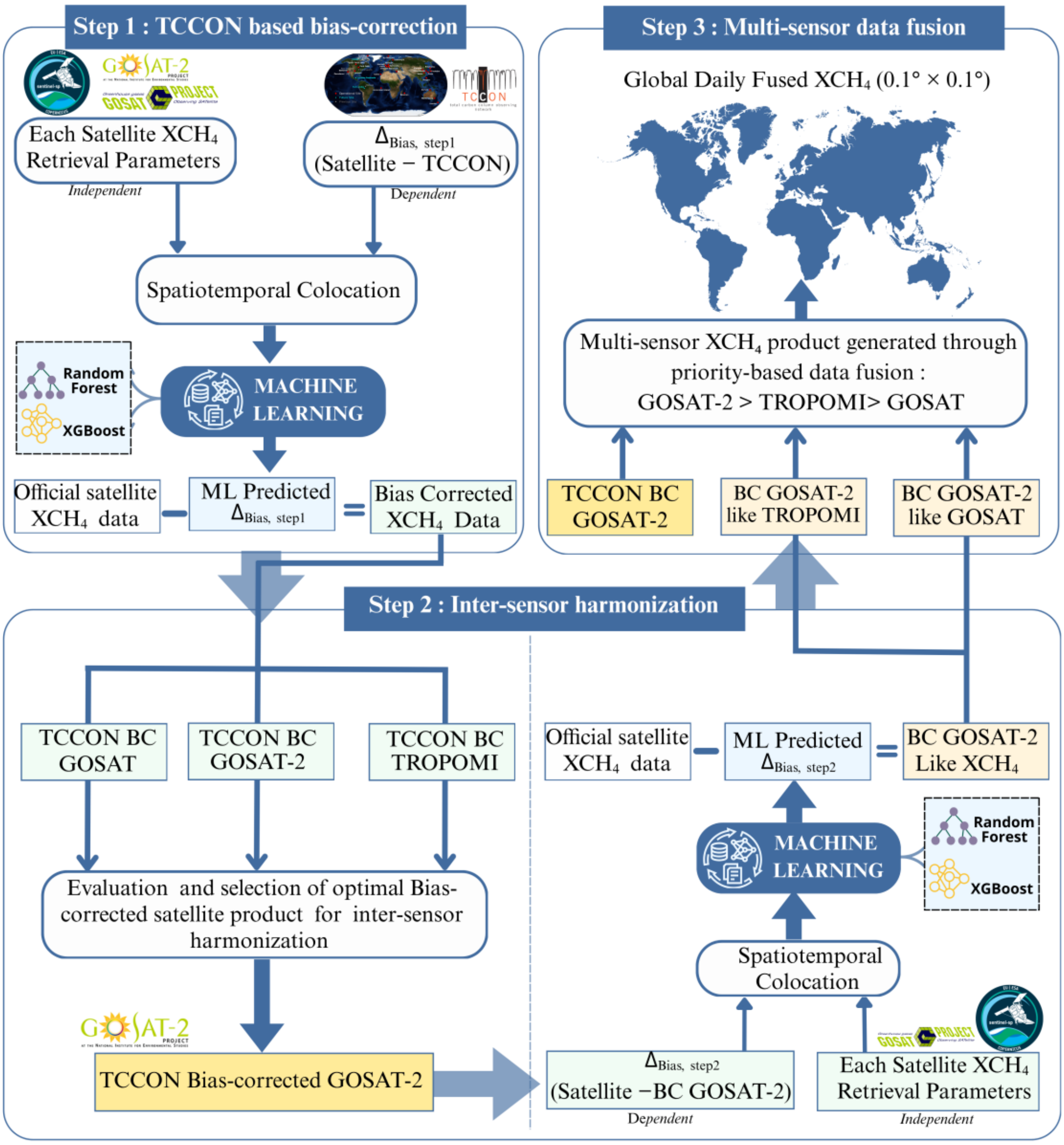

Figure 3. Overview of the machine learning (ML)-based bias correction (BC) and data fusion framework used to generate the Fused XCH_4 product.

3.1. Data preprocessing and colocation

Reliable colocation between satellite retrievals and reference observations is essential for bias correction and validation. The sparse global distribution of TCCON sites prevents perfectly coincident measurements (Zhou et al., 2016). We therefore constructed collocated training pairs using satellite-specific spatiotemporal and elevation constraints, adopting criteria from previous studies and official validation strategies (Balasus et al., 2023; Yoshida et al., 2023). Using the criteria in Table 3, we first established Step 1 between each satellite and TCCON. To ensure adequate temporal representation across 2020–2023 and sufficient training samples, TCCON sites with fewer than 20 collocated observations (i.e., bremen01, eureka01, nicosia01, and rikubetsu01) were excluded. We then constructed Step 2 inter-satellite colocations, pairing GOSAT and TROPOMI observations with TCCON calibrated GOSAT-2 using the thresholds in Table 3.

Table 3. Colocation criteria used for TCCON-based bias correction (Step 1) and inter-satellite harmonization (Step 2). All thresholds were chosen based on satellite-specific characteristics and standard validation practices.

Step	Reference	Satellite	Radius	Time window	Altitude difference
Step1	TCCON	GOSAT, GOSAT-2	200 km	±30 min	< 250 m
		TROPOMI	100 km	±1 hour	
Step2	Bias-corrected GOSAT-2	GOSAT	20 km	Same date	< 200 m
		TROPOMI	5 km	±1 hour	-

3.2. ML-based bias correction and harmonization

While GOSAT and TROPOMI provide official bias-corrected products (Inoue et al., 2016; Lorente et al., 2021), GOSAT-2 does not. To treat all sensors consistently, we developed a unified ML framework using TCCON as the calibration standard. Previous studies improved TROPOMI XCH_4 by aligning to GOSAT official (Fan et al., 2024) or GOSAT proxy data (Balasus et al., 2023; Li et al., 2024), which applies a single global offset to force mean bias to zero and is available only through 2021 (Parker et al., 2020). Our approach directly calibrates each sensor against TCCON, enabling spatially and temporally adaptive bias correction throughout 2020–2023 and data-driven harmonization reference selection.

3.2.1 Step 1: TCCON-based bias correction

For each satellite, we trained ML models using satellite–TCCON collocated pairs to predict the systematic bias between raw satellite retrievals and TCCON:

$$\Delta_{\text{Bias, step1}} = \mathrm{XCH}_{4,\text{Satellite}} - \mathrm{XCH}_{4,\text{TCCON}} \qquad (3)$$

Satellite-specific retrieval parameters were used as predictors to model systematic error in the raw XCH4 retrievals. Because each mission provides a large number of candidate retrieval parameters (>100), we applied a three-stage feature selection procedure:

1. Correlation screening: Pearson and Spearman analyses to rank predictors based on linear and monotonic associations with $\Delta_{Bias,\ step1}$.
2. Recursive feature elimination (RFE): RFE with cross-validation to identify a compact predictor subset.
3. Refinement: final adjustment using feature-importance rankings from preliminary models.

The final predictor lists are provided in Tables S1–S3. The trained model predicts $\hat{\Delta}_{Bias,\ step1}$, and the bias-corrected product is computed using Eq. (2).

3.2.2 Step 2: Inter-sensor harmonization

To select a harmonization reference, we evaluated the Step 1 bias-corrected outputs from all three sensors against common TCCON observations. GOSAT-2 exhibited the highest agreement with TCCON and was therefore selected as the harmonization reference (detailed results in Section 4.2). Using inter-satellite collocations (Table 3), we developed ML models to reduce sensor-to-sensor discrepancies relative to calibrated GOSAT-2:

$$\Delta_{Bias,\ step2} = XCH_{4,Satellite} - XCH_{4,BC\ GOSAT-2} \qquad (4)$$

where $XCH_{4,Satellite}$ is the standard retrieval from the target sensor (GOSAT or TROPOMI) and $XCH_{4\,,BC\;GOSAT-2}$ is the Step-1 bias-corrected GOSAT-2 retrieval. Feature selection followed the same three-stage procedure as in Section 3.2.1 (correlation screening, RFE, and importance refinement). Final predictor lists are provided in Tables S3–S4. We trained ML models to predict $\hat{\Delta}_{Bias,\ step2}$ and generated GOSAT-2-like harmonized products by subtracting the predicted bias:

$$XCH_{4\,,Harmonized} = XCH_{4,Satellite} - \hat{\Delta}_{Bias,\ step2} \qquad (5)$$

3.3. Step 3: Data Fusion

The fusion step integrates harmonized satellite datasets into a single daily 0.1° gridded product. We adopted a hierarchical priority-based fusion strategy (Chen et al., 2024), ranking datasets by their validation performance against TCCON and inter-sensor consistency. Because GOSAT-2 was selected as the harmonization reference and exhibits the strongest independent agreement with TCCON, it was assigned the highest priority. Based on the Step-2 evaluation, the final ranking used for fusion was:

GOSAT-2 (BC) → TROPOMI (GOSAT-2-like) → GOSAT (GOSAT-2-like)

For each day and each 0.1° grid cell *(x,y)*, the fused product was defined as:

$$XCH_{4,Fused}(x,y) = \begin{cases} XCH_{4,GOSAT-2}(x,y), & \textit{if available} \\ XCH_{4,TROPOMI}(x,y), & \textit{else if available} \\ XCH_{4,GOSAT}(x,y), & \textit{else if available} \\ NaN, & \textit{otherwise} \end{cases} \qquad (6)$$

This rule retains the highest-priority valid observation at each location and time, thereby improving both spatial coverage and precision of the fused daily XCH_4 product.

3.4 Model evaluation

The spatial and temporal generalization performance of the BC was quantitatively evaluated using step-specific validation strategies. In Step 1, spatial generalization was assessed using leave-one-site-out cross-validation (LOSOCV) to account for site-to-site differences in background XCH_4 levels and spatial heterogeneity. Temporal generalization was evaluated using leave-one-month-out cross-validation (LOMOCV) and leave-one-year-out cross-validation (LOYOCV) to account for interannual variability and growth trends (Jang et al., 2024). In Step 2, leave-one-band-out cross-validation (LOBOCV) was applied across 11 latitudinal zones (60°S–80°N; Fig. S1) to account for latitudinal gradients in CH_4 emissions (Maasakkers et al. 2019; Hwang et al., 2026), with temporal validation using LOMOCV and LOYOCV. Model performance was evaluated using three standard metrics: coefficient of determination (R^2), root mean square error (RMSE) and mean absolute error (MAE) (Equations S1–S3).

4 Results and discussion

4.1. Overall validation against TCCON

We evaluated the spatiotemporal generalization performance of official satellite products and ML-based bias-correction against TCCON. In Figure 4, LOSOCV results and TCCON observations were aggregated at each TCCON site to examine site-level mean bias, within-site variability, and station-to-station consistency. The standard products systematically deviated from the 1:1 line, with pronounced negative biases at low-XCH_4 sites such as Darwin01, Lauder03, and Sodankylä01 (Fig. 4a, d, g; see Fig. 1 for site locations). These sites are located in the Southern Hemisphere or high latitudes, where challenging retrieval conditions (e.g., high solar zenith angle and high surface albedo) and limited TCCON sampling can amplify errors.

In addition, operational bias corrections tuned around typical global XCH$_4$ levels (≈1850–1900 ppb) can leave larger residual deviations at the low and high tails.

In contrast, the ML-based correction tightened site-level agreement for all sensors, reducing both RMSE and MAE. This correction used sensor-specific models selected based on CV performance (Table S5; XGBoost for TROPOMI, RF for GOSAT and GOSAT-2). For TROPOMI, the RMSE decreased from 14.26 ppb (standard) and 5.49 ppb (operational bias-corrected) to 3.28 ppb (ML), corresponding to reduction of 73% and 40%, respectively (Fig. 4a–c). For GOSAT, RMSE reductions of 54% and 45% were achieved relative to the operational standard and bias-corrected products, respectively, while GOSAT-2 showed a 41% reduction relative to the operational standard (Fig. 4d–h). Site-wise error statistics (Figs. S2–S4) confirmed these improvements, with ML-based correction reducing both station-wise mean bias (μ) and variability (σ), indicating more uniform performance under spatially heterogeneous conditions. Given a global XCH$_4$ growth rate of ~8–14 ppb yr^{-1} during the study period (NOAA GML; https://gml.noaa.gov/ccgg/trends_ch4/; last accessed 26 December 2025), these reductions are large enough to influence long-term trend interpretation.

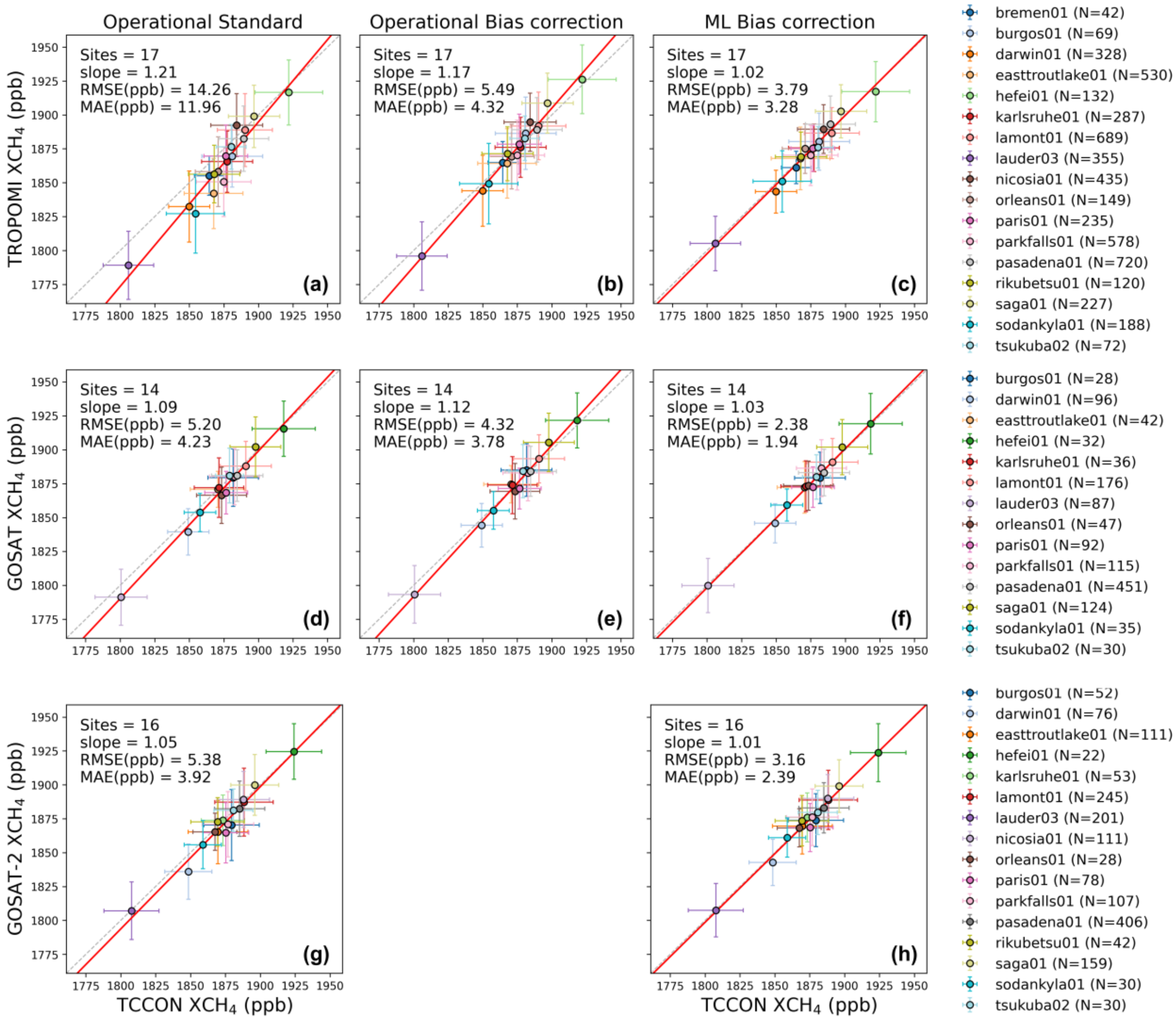

Figure 4. Site-wise scatterplots of column-averaged dry-air methane (XCH$_4$) between Total Carbon Column Observing Network (TCCON) and satellite products; (a–c) TROPOMI XCH$_4$, (d–f) GOSAT XCH$_4$, (g–h) GOSAT-2 XCH$_4$ for the operational standard and operational bias-corrected products, and machine learning (ML) based bias-corrected result (under leave-one-site-out cross-validation), respectively. Each marker represents the mean XCH$_4$ at one TCCON site over the study period (2020–2023), with horizontal and vertical error bars indicating one standard deviation of TCCON and satellite XCH$_4$, respectively. Red lines denote least-squares linear regression fits.

The LOMOCV results further highlighted differences in temporal generalization (Fig. 5). Across sensors, the standard products showed negative biases and broad interquartile ranges (IQRs) throughout the year, with strong negative shifts from June to

September. The seasonal aggregation confirmed that this negative bias was most pronounced in June-July-August (JJA). This seasonal pattern is consistent with known sensitivities of SWIR-based XCH_4 retrievals to surface albedo and atmospheric scattering by aerosols and cirrus (Inoue., 2016; Hu et al., 2016; Lorente et al., 2021; Oshio et al., 2020). These factors can modify the effective light path and vary seasonally with vegetation, humidity, cloud conditions, and solar geometry. Operational bias correction shifted the median bias toward zero but still exhibited larger seasonal dispersion than the ML-based correction. The ML-based correction maintained seasonal medians near zero and reduced both the IQRs and non-outlier spread, with most IQRs remaining within ±8 ppb, indicating more stable performance under seasonal variability.

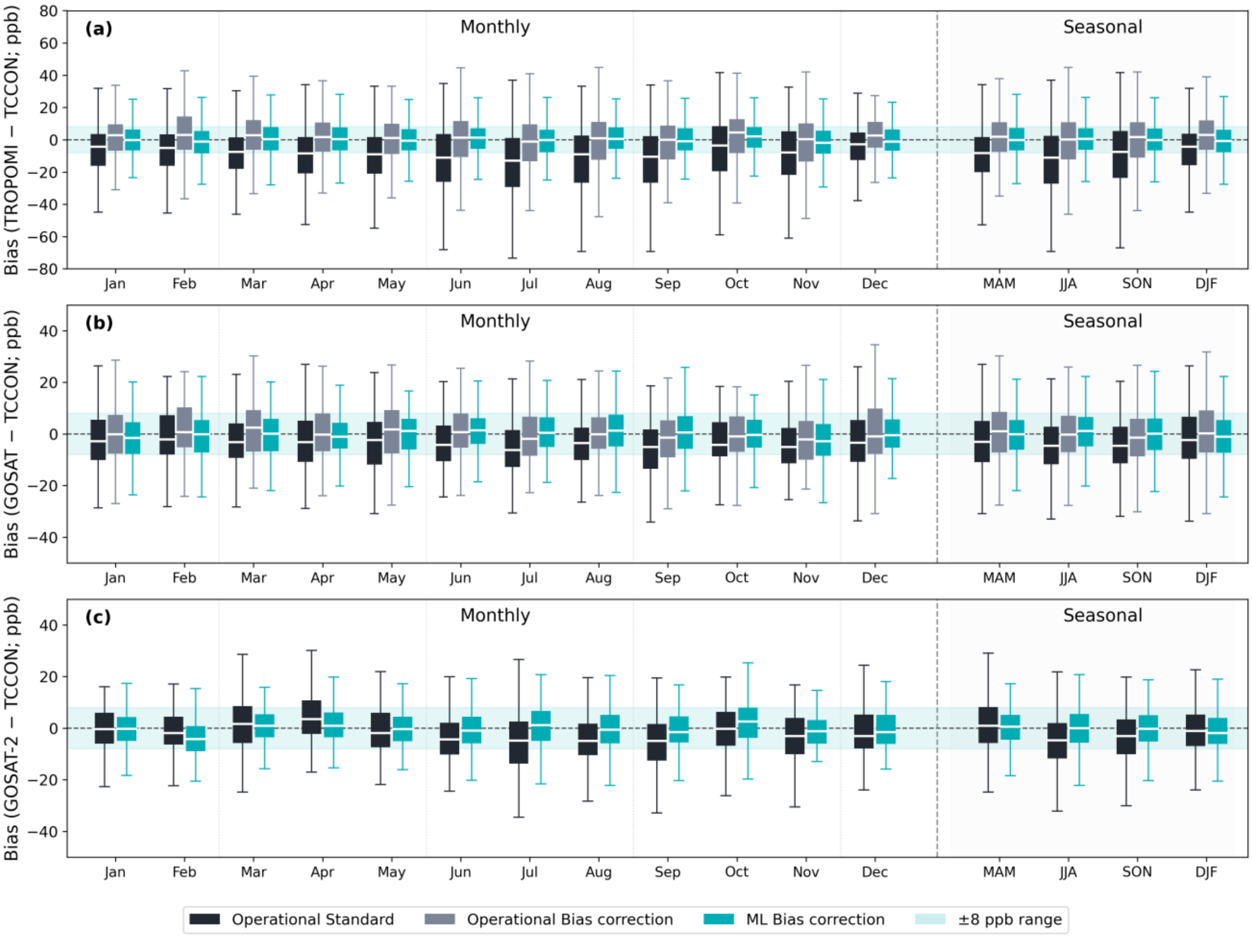

Figure 5. Monthly and seasonally aggregated XCH_4 bias distributions under leave-one-month-out cross-validation (LOMOCV). Box-and-whisker plots show bias distributions (Satellite − TCCON) for each calendar month and their seasonal aggregations for (a) TROPOMI, (b) GOSAT, and (c) GOSAT-2. The compared datasets include the uncorrected operational standard products, operational bias-corrected products, and ML-based bias-corrected results. Boxes indicate the interquartile range (IQR) with the median shown as a horizontal white line. The shaded band marks the ±8 ppb range around zero bias.

Figure 6 further illustrates condition-dependent biases by relating the XCH_4 ratio (TCCON/ satellite) to key retrieval variables. For TROPOMI, the standard product shows a strong negative dependence on SWIR surface albedo ($R = -0.49$; Fig. 6a), consistent with known sensitivity to scattering-related light-path errors under low-albedo conditions (Lorente et al., 2021; Balasus et al., 2023; Li et al., 2024). Bias correction substantially reduces this dependence (Fig. 6b), yielding near-zero correlation ($R = -0.02$) and indicating that albedo-driven bias is largely mitigated. For the GOSAT series, operational bias correction is implemented as a multiple linear regression using explanatory variables (e.g., ΔPs, XH_2O, airmass, and ΔT) (Inoue et al., 2016; Yoshida et al., 2023). Consistently, ΔPs dependence is weak for GOSAT ($R = 0.22$; Fig. 6c) and more evident for GOSAT-2 ($R = 0.35$; Fig. 6e) in the standard products, and it is reduced after correction (Fig. 6d, f). Overall, the ML-based correction reduces not only mean bias but also bias sensitivity to key retrieval conditions across sensors.

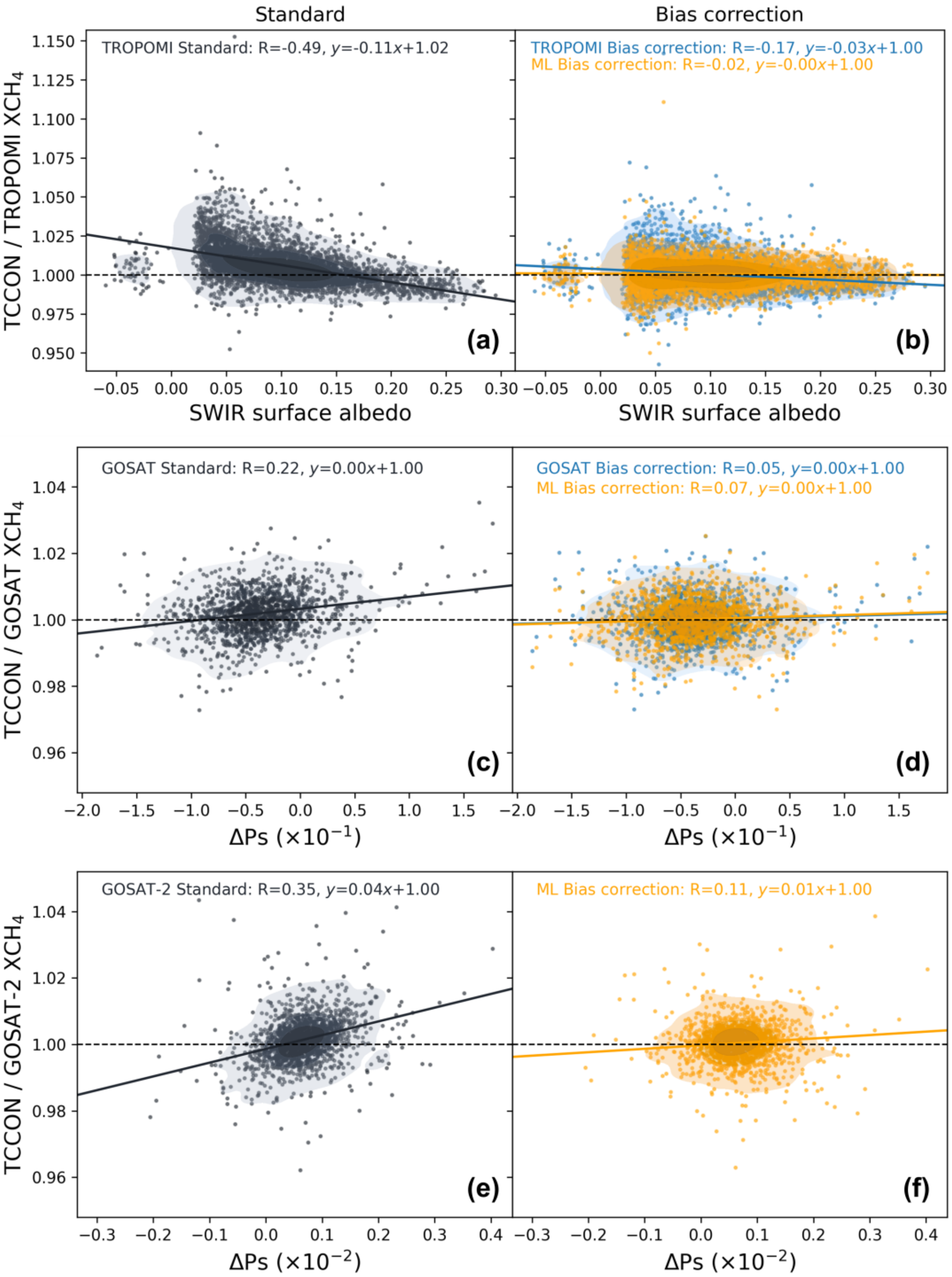

Figure 6. Dependence of (TCCON/Satellite) XCH_4 ratios on key retrieval variables and its reduction after bias correction. (a,b) (TCCON/TROPOMI) XCH_4 ratio as a function of SWIR surface albedo for the standard product (a) and after bias correction (b). (c–f) Same as (a,b) but for GOSAT and GOSAT-2 as a function of surface pressure difference (ΔPs): standard product in (c,e) and bias-corrected results in (d,f). Solid lines denote the fitted least-squares regressions, and the dashed horizontal line indicates the unbiased reference level (ratio = 1). The Pearson correlation coefficient (R) and regression equation are reported in each panel.

4.2. Inter-satellite harmonization

Multi-sensor fusion requires minimizing inter-sensor inconsistencies by defining a common reference scale. Table 4 compares the ML-based bias-corrected products from all three sensors evaluated against TCCON using common collocated samples under LOSOCV, ensuring that the reference selection is based on independent out-of-site performance. GOSAT-2 achieved the highest accuracy ($R^2 = 0.67$; RMSE = 10.67 ppb) and was therefore selected as harmonization reference.

Table 4. Accuracy comparison of machine learning (ML) based bias-corrected XCH$_4$ from three satellites sensors (TROPOMI, GOSAT, GOSAT-2), evaluated against TCCON using common collocated samples (N = 309) under leave-one-site-out cross-validation. Boldface indicates the satellite with the best performance for each error metric.

Metrics	TROPOMI	GOSAT	GOSAT-2
R^2	0.60	0.60	**0.67**
MAE (ppb)	9.49	9.21	**8.38**
RMSE (ppb)	11.78	11.92	**10.67**

To improve cross-sensor consistency, the GOSAT and TROPOMI products were calibrated to the ML-based bias-corrected GOSAT-2 scale (i.e., generating "GOSAT-2-like" XCH$_4$). Across the evaluated algorithms, XGBoost yielded the best harmonization performance (Table S6). Figure 7 shows distributional shifts before and after harmonization: after harmonization, bias distributions for GOSAT and TROPOMI moved toward near-zero mean bias relative to GOSAT-2 and their spread was reduced. This inter-sensor harmonization further assessed the major retrieval-parameter dependencies identified in the TCCON-based analysis over broader parameter ranges (Fig. 8). After ML-based harmonization, the SWIR surface albedo dependency of TROPOMI and the ΔPs dependency of GOSAT were nearly removed, indicating improved consistency with the ML-based bias-corrected GOSAT-2 scale.

After harmonization, TROPOMI exhibited slightly higher agreement with GOSAT-2 (Table S6) than GOSAT and provided approximately six times more collocated observations (183,550 for TROPOMI vs. 32,244 for GOSAT). Accordingly, the fusion priority was set to GOSAT-2 → TROPOMI → GOSAT to balance reference consistency and sampling density and to enhance robustness of the fused XCH$_4$ product. Finally, we generated a daily 0.1° fused XCH$_4$ product by integrating the harmonized observations from the three satellites.

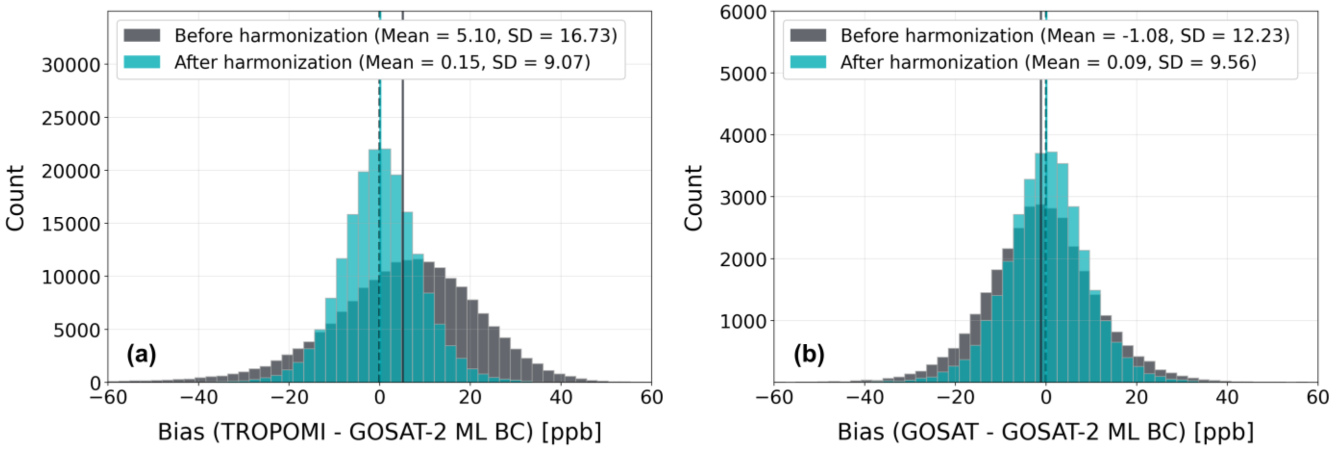

Figure 7. Inter-satellite harmonization to the ML bias-corrected GOSAT-2 ML BC scale. Distributions of XCH$_4$ bias relative to the ML-based bias-corrected GOSAT-2 product ((a): TROPOMI − GOSAT-2; (b): GOSAT − GOSAT-2) before and after cross-satellite harmonization. Solid vertical lines denote the mean bias for each distribution, and the legend reports the corresponding mean and standard deviation (SD).

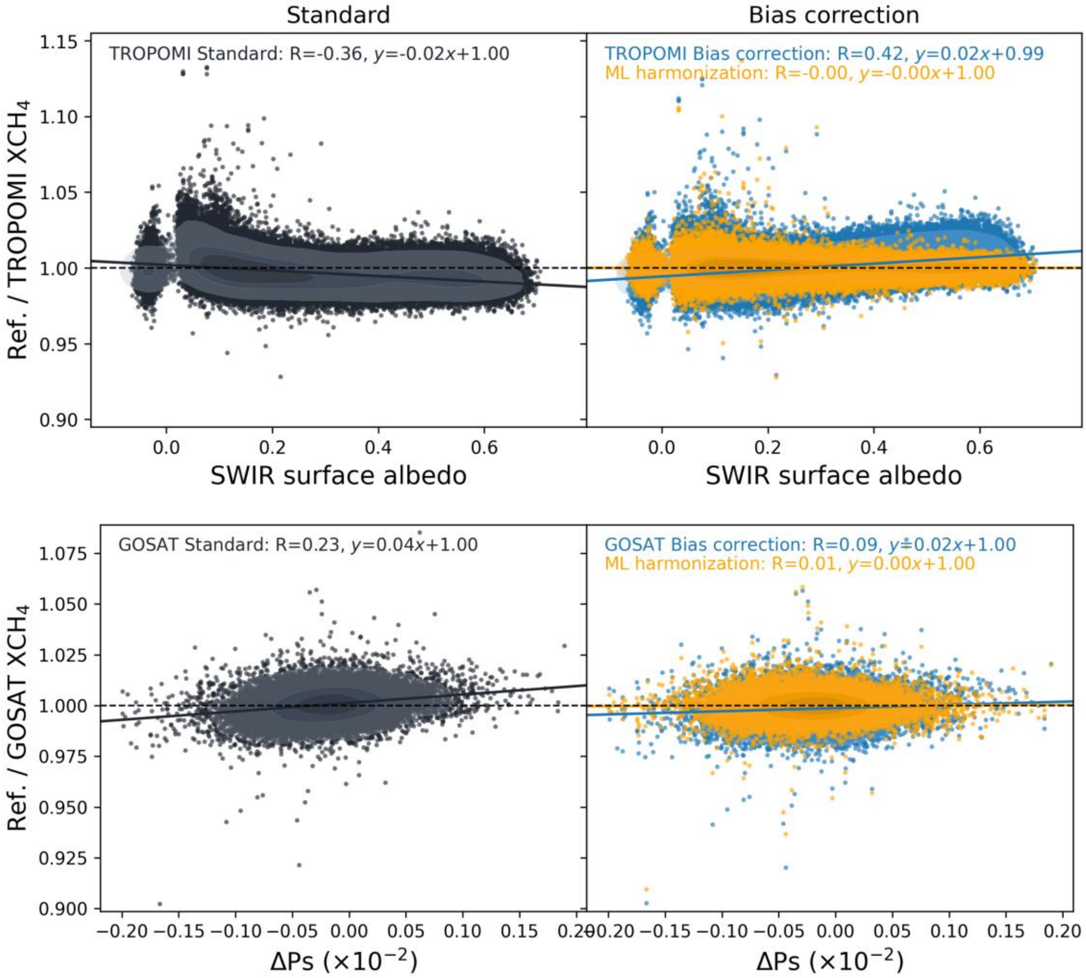

Figure 8. Retrieval-parameter dependency of harmonized XCH$_4$ relative to the final target. Scatter density plots show the ratio of satellite XCH$_4$ to the final target, defined as the ML-based bias-corrected GOSAT-2 XCH$_4$, as a function of key retrieval parameters using satellite co-location samples. The upper panels show the dependency of TROPOMI XCH$_4$ on SWIR surface albedo, and the lower panels show the dependency of GOSAT XCH$_4$ on the surface pressure difference, ΔPs. For each sensor, the left panels show the standard products, while the right panels compare the operational bias-corrected products and the ML-based harmonized results.

Figure 9 evaluates the fused XCH$_4$ product at three independent TCCON sites (Xianghe01, Edwards01, and Garmisch01) and includes a comparison with the Blended TROPOMI+GOSAT XCH$_4$ product of Balasus et al. (2023). These sites were excluded from the TCCON-based bias correction in Step 1 to assess generalization under independent conditions. The three stations represent distinct environments: a peri-urban site influenced by strong anthropogenic emissions (Xianghe, China; mean = 1903.16 ppb), an arid high-desert site with high surface albedo (Edwards, USA; mean = 1880.37 ppb), and a mountainous site (Garmisch, Germany; mean = 1872.98 ppb). Across all sites, the fused XCH$_4$ showed strong agreement with TCCON (R^2 = 0.81, RMSE = 10.78 ppb; Fig. 9a). The time series further indicates that the fused product reproduces temporal variability, while reducing inter-sensor offsets relative to the individual satellite products (Fig. 9b). For 2022, the fused product achieved higher accuracy than the Blended XCH$_4$ product at the same locations, (R^2 = 0.74, RMSE = 10.38 ppb vs. R^2 = 0.67, RMSE = 11.82 ppb; Fig. 9c), which may reflect the use of a harmonized multi-sensor framework that incorporates the higher-accuracy GOSAT-2 product.

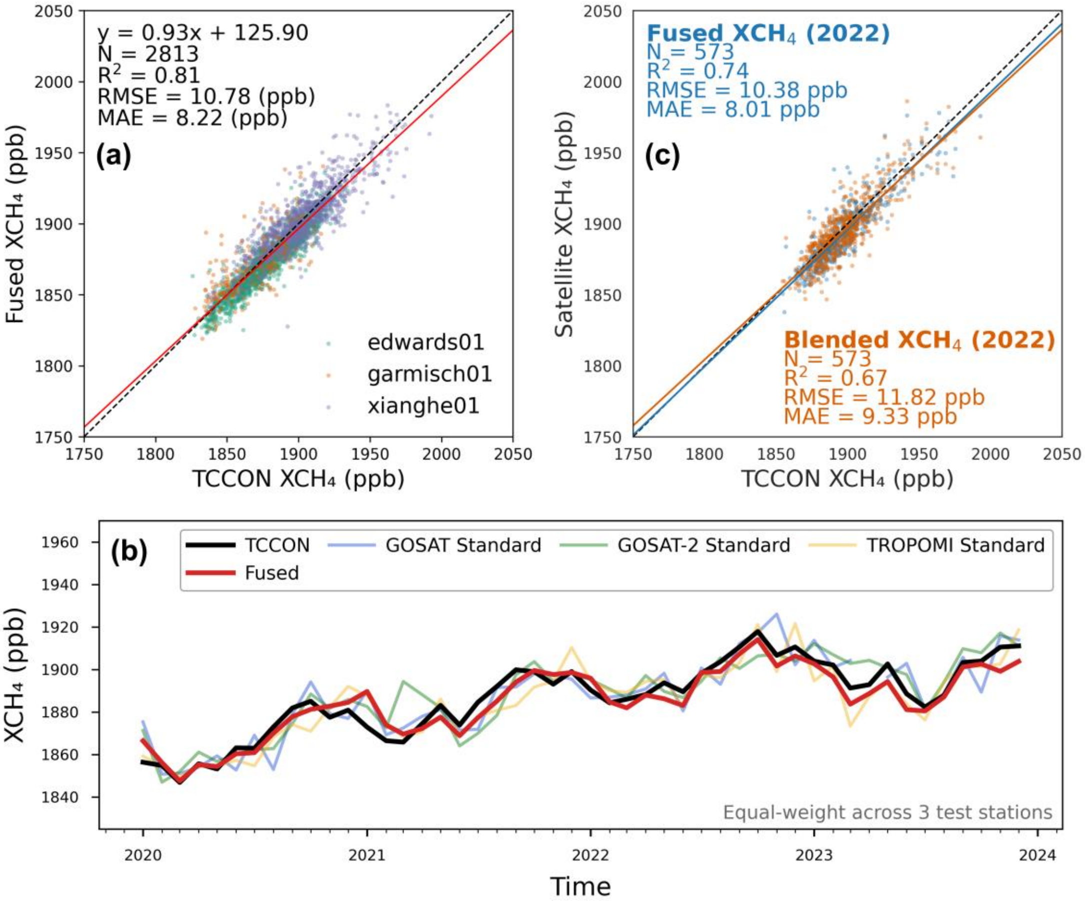

Figure 9. Independent validation of the Fused XCH_4 at three TCCON test stations and comparison with a Blended product (Balasus et al., 2023). (a) Scatter plot of Fused XCH_4 versus TCCON XCH_4 at three independent sites (Xianghe01, Edwards01, and Garmisch01); colors indicate individual stations. The red line denotes the fitted regression. (b) Time series of station-mean XCH_4 averaged across the three test stations (equal-weight mean), comparing TCCON, Fused, and the standard products from GOSAT, GOSAT-2, and TROPOMI. (c) Comparison against TCCON for 2022 at the same test stations, contrasting the Fused XCH_4 (blue) with the Blended XCH_4 product based on TROPOMI and GOSAT (orange). The solid-colored lines denote fitted regressions, respectively.

4.3. Coverage improvements from multi-satellite fusion

The fused XCH_4 product achieved annual global land coverage of 87.1%, 86.9%, 86.8%, and 88.1% for 2020–2023, corresponding to improvements of 0.45–0.74 percentage points over TROPOMI alone (Fig. S5a). Although global annual averages show modest gains, multi-sensor fusion yields substantial regional enhancements where individual sensors face systematic retrieval limitations.

To quantify fusion benefits under challenging retrieval conditions for TROPOMI, we examined five case-study regions (ROIs; see Fig. 1) in 2023 representing diverse environments and emission regimes: South Asia (ROI-A) and the Amazon Basin (ROI-B) as cloudy tropical regions with aerosol impacts; Eastern Siberia (ROI-C) as high-latitude wetlands with seasonal snow/ice constraints; the Pacific Northwest (ROI-D) as complex coastal terrain; and Central Europe (ROI-E) as Alpine topography (Fig. 10) . Compared with TROPOMI, coverage improvements ranged from ~2.5% to ~9.5%, with the largest gain in South Asia (Fig. 10a). Source attribution maps illustrate how the GOSAT series spatially complements TROPOMI coverage in 2023 (Fig. 10b): GOSAT-2 provides the majority of additional observations, particularly filling monsoon-related gaps in South Asia and cloudy tropical regions, while GOSAT supplements coverage over Alpine terrain, where complex topography challenges both TROPOMI and GOSAT-2 retrievals.

Fusion also improves temporal resilience during periods of single-mission data loss. Missing VIIRS cloud-screening information in July–August 2022 and August 2023 (Borsdorff et al., 2024) led to substantial gaps in TROPOMI XCH_4, which were partially filled by overlapping GOSAT and GOSAT-2 observations (Fig. S5b). This multi-sensor complementarity highlights the importance of global-scale fusion for comprehensive CH_4 monitoring.

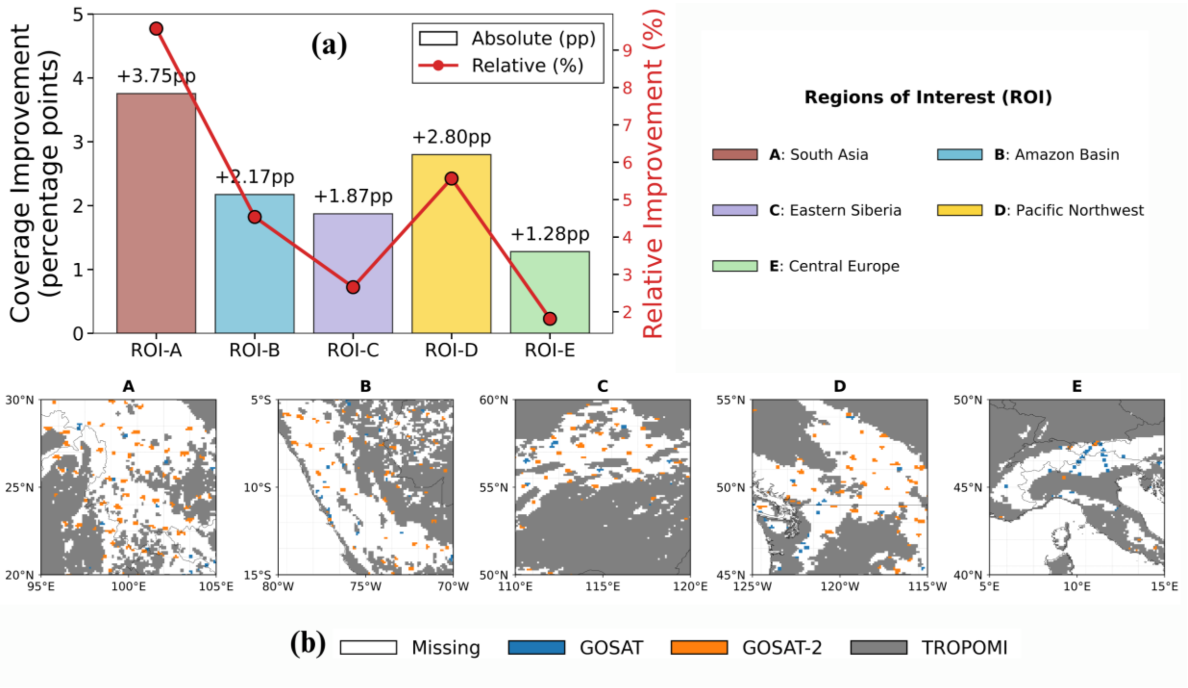

Figure 10. Regional assessment of multi-sensor XCH_4 fusion benefits in 2023 across five regions representing distinct retrieval challenges. (a) Coverage enhancement relative to TROPOMI showing absolute gain in percentage points (bars, left axis) and relative improvement (line, right axis). (b) Annually dominant sensor per pixel based on valid retrieval frequency in 2023 for each ROI (GOSAT: blue, GOSAT-2: orange, TROPOMI: grey, missing data: white). Orange and blue pixels indicate locations where TROPOMI data are unavailable but coverage is provided by GOSAT-2 or GOSAT

4.4. Global XCH4 mapping and spatiotemporal analysis

The fused dataset reveals distinct spatiotemporal patterns across 2020–2023. Time–latitude diagrams (Fig. 11a) show a persistent interhemispheric gradient of 30–40 ppb between the Northern Hemisphere (NH) and Southern Hemisphere (SH). Elevated XCH_4 is consistently observed in the northern subtropical belt (0–40°N), where mean concentrations increased from 1872.72 ppb to 1906.98 ppb over the study period (+34.26 ppb), exceeding the global mean increase. While the highest concentrations remained in the north, the fused product captured a progressive southward expansion in XCH_4 increases beginning in 2021, consistent with recent findings (Umezawa et al., 2025).

To quantify global growth rates, we compared the monthly global average of the fused XCH_4 dataset with independent observations from TCCON ground-based XCH_4 measurements and NOAA marine surface CH_4 records (https://gml.noaa.gov/ccgg/trends_ch4/, last accessed: 26 December 2026). Mean annual growth rates were calculated from the monthly time series over 2020–2023, while uncertainties represent the variability of monthly growth rates within each year. The fused product captures a sustained increase from approximately 1850 ppb in early 2020 to nearly 1900 ppb by late 2023, corresponding to a mean global growth rate of 12.28 ± 1.00 ppb yr^{-1} (Fig. 11b). This agrees well with TCCON (13.56 ± 1.25ppb yr^{-1}) and NOAA (14.77 ± 0.64ppb yr^{-1}), supporting the ability of the fused dataset to represent large-scale atmospheric CH_4 variability and interannual trends.

Interannual growth rates exhibited strong regional variability (Fig. 11c). The NH (0–80°N), SH (60°S–0°), and the high-emission zone (0–40°N) all peaked in 2021 at 14.3 ± 2.2, 15.4 ± 2.7, and 15.5 ± 2.1ppb yr^{-1}, respectively, consistent with record global XCH_4 increases reported for that period (Saunois et al., 2025). Following this peak, growth rates generally declined during 2022–2023, reaching approximately 6.0 ± 1.8ppb yr^{-1} in the NH, 11.4 ± 3.9ppb yr^{-1} in the SH, and 6.4 ± 3.0ppb yr^{-1} in the high-emission zone by 2023, consistent with recent inverse modeling estimates (Pendergrass et al., 2025).

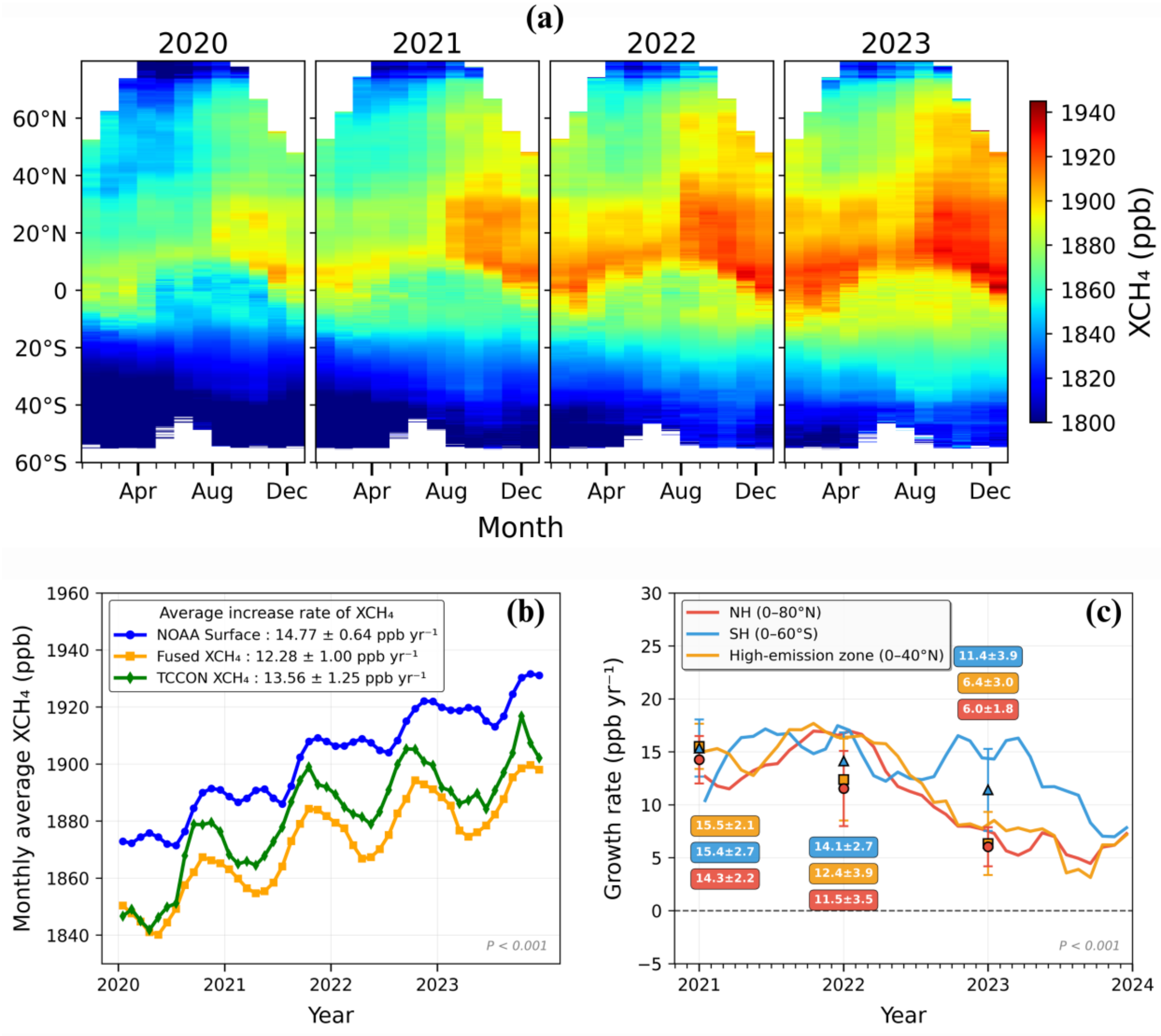

Figure 11. Spatiotemporal characteristics and growth of fused XCH_4 during 2020–2023. (a) Monthly latitudinal distribution of fused XCH_4 concentrations at 0.1° spatial resolution from 2020 to 2023. (b) Comparison of monthly global mean methane time series from the fused XCH_4 product (orange), NOAA marine surface CH_4 measurements (blue), and TCCON ground-based XCH_4 observations (green). Values in the legend indicate mean annual growth rates over 2020–2023 with associated uncertainties. (c) Monthly hemispheric year-over-year differences (solid lines) and annual mean growth rates (markers) for the Northern Hemisphere (NH; 0–80°N, red), Southern Hemisphere (SH; 0–60°S, blue), and high-emission zone (0–40°N, orange). Error bars represent the standard deviation of monthly growth rates within each year. All trends shown in panels (b) and (c) were statistically significant ($p < 0.001$).

To highlight emission hotspots relative to the global baseline, we computed annual anomalies by subtracting the four-year mean (1869.95 ppb) from each year's XCH_4 field (Fig. 12). By 2023, positive anomalies exceeding +60 ppb were apparent over South Asia, East Asia, and Central Africa, with maxima over the Indo-Gangetic Plain and the Ganges–Brahmaputra delta (Fig. 12d). The shift in global mean anomaly from −16.74 ppb (2020) to +14.16 ppb (2023) indicates increasing XCH_4 accumulation over the study period.

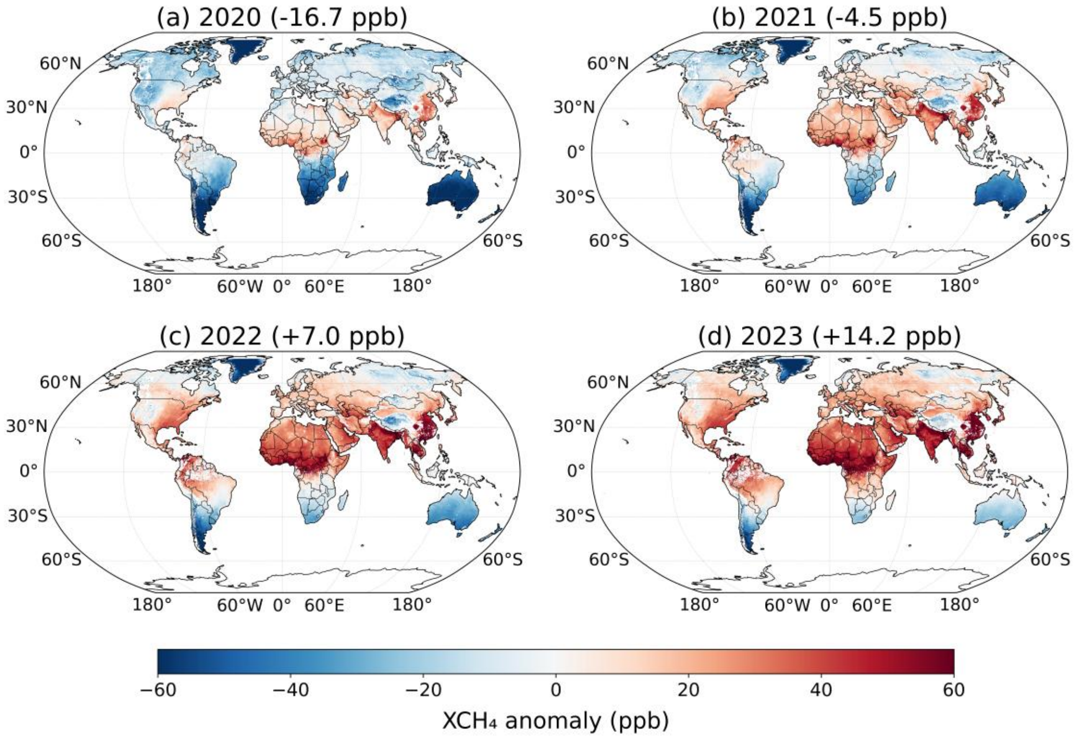

Figure 12. Annual XCH_4 anomaly maps for (a) 2020, (b) 2021, (c) 2022, and (d) 2023 relative to the four-year mean. Parentheses show global mean anomalies (ppb). Positive (red) and negative (blue) shading indicate regions with XCH_4 above and below the four-year baseline, respectively.

To interpret drivers of elevated concentrations, we examined high-anomaly regions in 2023 using MODIS MCD12Q1 land-cover information (Fig. 13). Hotspots showed distinct land-cover signatures: the Niger Delta (a) exhibited strong anomalies over a mix of croplands, evergreen broadleaf forests, coastal wetlands, and urban areas associated with petroleum infrastructure (Sj et al., 2024); the Ganges–Brahmaputra Delta (b) showed the largest anomaly over rice paddies and permanent wetlands; the Indo-Gangetic Plain (c) and Yangtze River Delta (d) displayed persistent enhancements over irrigated croplands and expanding metropolitan areas; the Congo Basin (e) showed elevated concentrations over tropical peatlands and evergreen forests; and the southern United States (f) showed enhancements over the Permian Basin, consistent with documented oil-and-gas emissions (Zhang et al., 2020). The spatial correspondence between enhanced XCH_4 and wetland/cropland/urban land classes demonstrates the fused product’s ability to resolve regional emission patterns.

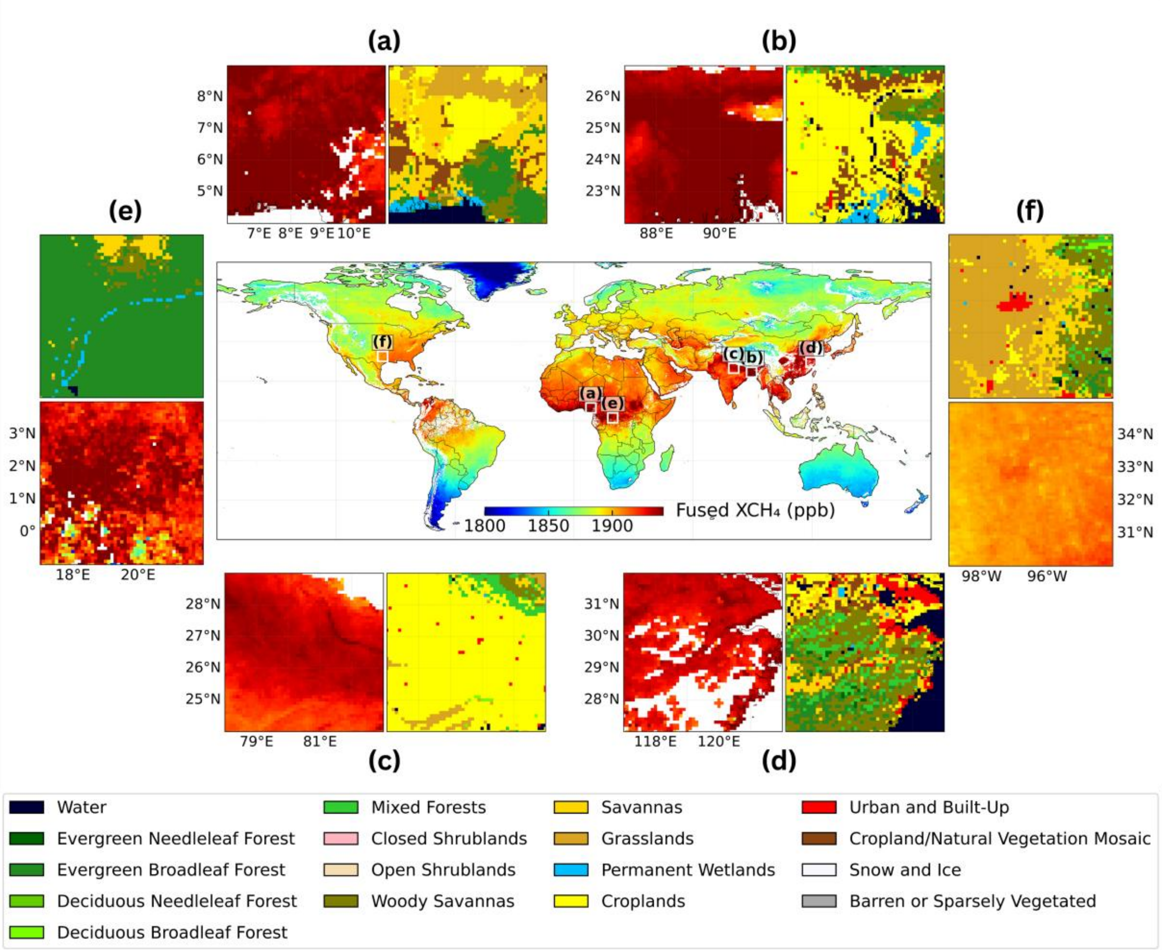

Figure 13. Regional XCH_4 emission hotspots and corresponding land-cover characteristics for 2023. The central map displays the global distribution of fused XCH_4 concentrations with six representative high-emission regions marked (a–f). Each regional panel pair shows XCH_4 concentrations (left) and MODIS MCD12Q1 land-cover classifications (right) for the Niger Delta (a), Ganges–Brahmaputra Delta (b), Indo-Gangetic Plain (c), Yangtze River Delta (d), Congo Basin (e), and southern United States (f). Land-cover legend follows the MODIS MCD12Q1 LC_Type1 classification.

Finally, we examined seasonal patterns of global XCH_4 in 2023. To preserve localized XCH_4 enhancements, zonal-mean profiles were calculated at native 0.1° latitude resolution (Fig. 14), and seasonal statistics were summarized for major latitude zones (Table S7). The NH (0–80°N) exhibited the largest seasonal amplitude (32.14 ppb), peaking in winter (DJF; 1915.36 ppb) and reaching a minimum in spring (MAM; 1883.22 ppb). Within the NH, the high-emission zone (0–40°N) remained consistently elevated throughout the year, ranging from approximately 1901 ppb in JJA to approximately 1918 ppb in SON/DJF, with a moderate seasonal amplitude of 16.50 ppb. In contrast, the SH (60°S–0°) showed a smaller amplitude (6.77 ppb), varying between 1850.66 ppb in MAM and 1857.43 ppb in JJA. The pronounced NH seasonality reflects strong source variability from wetland and agricultural emissions, whereas the smoother SH cycle is more strongly governed by the OH sink than by local emissions (East et al., 2024).

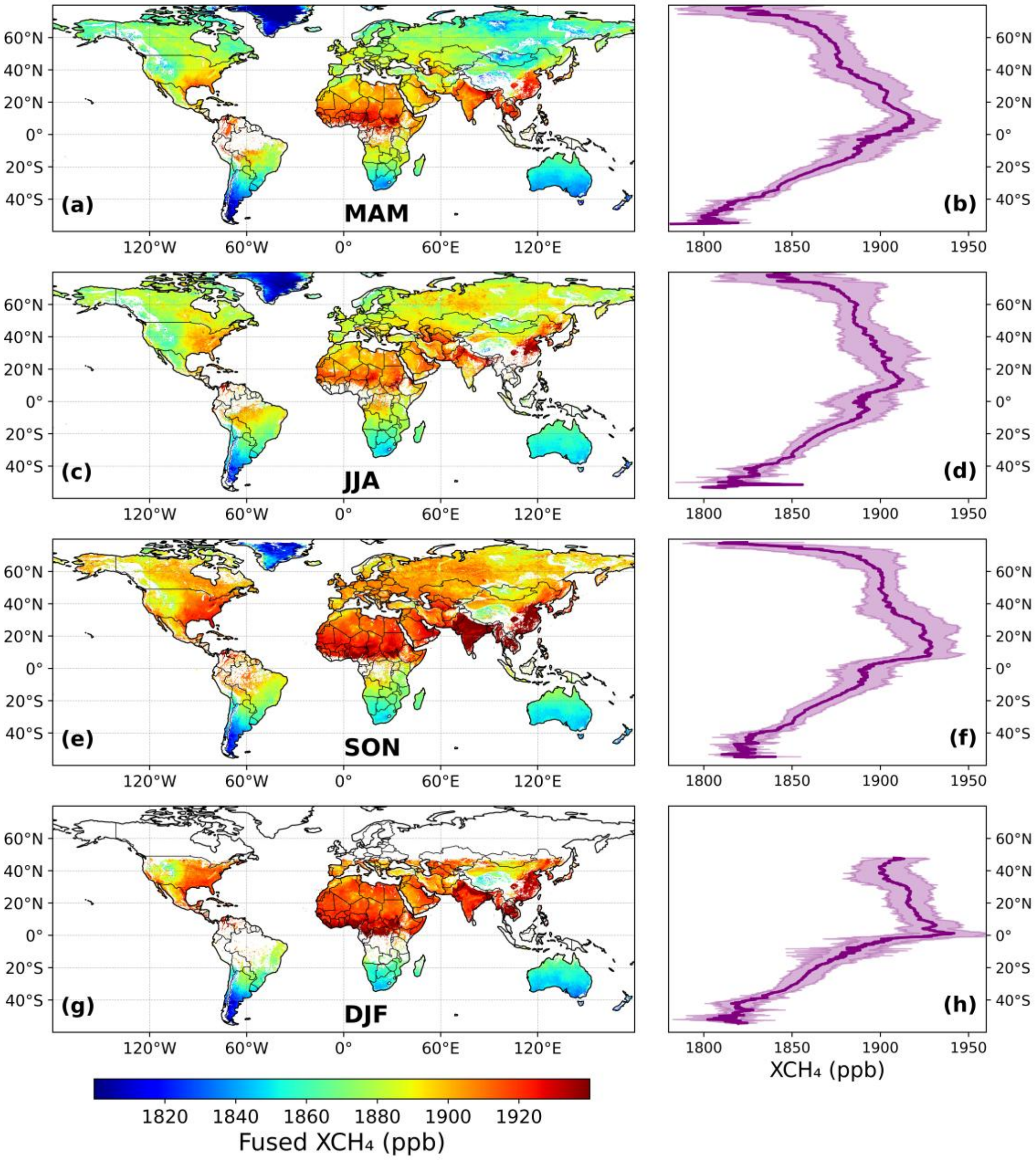

Figure 14. Seasonal distributions of fused XCH_4 concentrations and latitudinal gradients in 2023. Left panels (a, c, e, g) show seasonal mean XCH_4 concentrations at 0.1° resolution for March–April–May (MAM), June–July–August (JJA), September–October–November (SON), and December–January–February (DJF). Right panels (b, d, f, h) display corresponding zonal mean profiles (solid purple line) with shaded regions representing spatial variability (±1σ standard deviation) across each latitude band. Latitudes with data coverage below 2% were excluded from zonal mean calculations to ensure statistical robustness. Regional definitions and seasonal statistics are detailed in Table S7.

4.5. Limitations

While the framework substantially improves retrieval accuracy across sensors, several limitations should be noted. First, the ML-based bias correction relies on TCCON as the primary reference dataset. Although TCCON provides high-precision ground-based XCH_4 observations, its spatial distribution is limited and does not fully represent the diverse retrieval conditions encountered globally, particularly high-surface-albedo conditions. We partly addressed this limitation through LOSOCV strategy and additional satellite match-up analyses over broader surface albedo ranges, but independent validation under underrepresented retrieval conditions remains necessary. Second, the fused dataset uses a fixed sensor-priority strategy (GOSAT-2 → TROPOMI → GOSAT) based on overall accuracy and sampling density, which may introduce regional bias because local observing conditions can favor a non-prioritized sensor. Third, although the fusion framework improves robustness, global annual coverage gains are modest (0.45–0.74 percentage points over TROPOMI). Forth, ML-based correction in this study relies primarily on retrieval parameters to model systematic biases; incorporating external environmental covariates (e.g., temperature, humidity, and wind) may further reduce regional biases and improve generalization (Qu et al., 2025). Finally, the 0.1° resolution supports regional-scale analyses but remains insufficient for resolving fine-scale emission sources detectable by emerging high-resolution missions (e.g., EMIT or GHGSat). Future work could address these limitations via adaptive sensor weighting, uncertainty quantification, and integration of additional environmental covariates.

5 Conclusion

This study presents the first global multi-sensor fusion framework that integrates XCH_4 retrievals from GOSAT, GOSAT-2, and TROPOMI. Using a three-step ML strategy (1) TCCON-calibrated bias correction (2) inter-sensor harmonization, and (3) fusion, we produced a globally harmonized daily 0.1° land XCH_4 dataset for 2020–2023. Independent evaluation at withheld TCCON sites demonstrates strong generalization ($R^2 = 0.81$, RMSE = 10.78 ppb), outperforming the standard and operationally bias-corrected satellite products.

A key outcome is that GOSAT-2 provides an effective anchor for cross-sensor harmonization, offering high agreement with TCCON while maintaining broader sampling than GOSAT. The bias-correction and harmonization analyses also revealed and mitigated sensor-specific residual bias structures, including the SWIR surface albedo dependency in TROPOMI and the ΔPs dependency in GOSAT. These results indicate that the proposed framework not only improves the final fused product but also provides diagnostic insight into retrieval-condition-dependent limitations of the individual satellite products.

Regional assessments show that fusion improves data availability in retrieval-limited environments, increasing coverage by ~2.5% to ~9.5% depending on the region compared to the TROPOMI operational product. Although the overall global coverage gain is modest, the fused product provides complementary XCH_4 information in regions or conditions where TROPOMI retrievals are limited.

The fused product reproduces key spatiotemporal characteristics of atmospheric XCH_4, including interannual hemispheric variability and persistent emission hotspots in tropical and subtropical regions associated with wetlands, agriculture, and fossil-fuel infrastructure. The dataset can support downstream applications such as XCH_4 gap filling, multi-sensor intercomparison and harmonization, regional methane assessment, hotspot identification, and the development of advanced fusion strategies. The sensor-specific corrected and harmonized products can also serve as reference-scale benchmarks for future XCH_4 bias-correction studies. The proposed framework is extensible to upcoming missions (GOSAT-GW, CO2M), enabling enhanced monitoring. Continued advances in multi-sensor harmonization and uncertainty characterization will be crucial for supporting progress toward the GMP target of a 30% CH_4 emission reduction by 2030.

Code and data availability

The publicly available dataset includes the daily globally harmonized fused XCH_4 product at 0.1° spatial resolution for 2020–2023, individual harmonized gridded products used in the fusion process (TCCON bias-corrected GOSAT-2, GOSAT-2-like harmonized TROPOMI, and GOSAT-2-like harmonized GOSAT), and source sensor identifiers indicating which satellite contributed each valid observation in the fused product. All products are provided in HDF5 format and are available on Zenodo at https://doi.org/10.5281/zenodo.20304047. The fusion pipeline and example usage code for working with the dataset are available at https://github.com/jnkeya/Fused_XCH4. All input datasets used in this study are publicly available as described in Sect. 2.

Author contributions

J.K.: Writing – original draft, Visualization, Validation, Methodology, Investigation, Formal analysis, Conceptualization. Y.K.: Writing – original draft, Visualization, Validation, Methodology, Investigation, Formal analysis, Conceptualization. H.C.: Writing – review & editing. J.I.: Writing – review & editing, Supervision, Methodology, Funding acquisition, Conceptualization.

Competing interest

The authors declare that they have no conflict of interest.

Acknowledgments

This work was supported by Korea Environment Industry & Technology Institute (KEITI) through Project for developing an observation-based GHG emissions geospatial information map, funded by Korea Ministry of Environment (MOE) (RS-2023-00232066). Y. Kim were partially supported by Basic Science Research Program through the National Research Foundation of Korea (NRF), funded by the Ministry of Education (RS-2024–00408905).

References

ACP - Global distribution of methane emissions, emission trends, and OH concentrations and trends inferred from an inversion of GOSAT satellite data for 2010–2015: https://acp.copernicus.org/articles/19/7859/2019/, last access: 23 April 2026.

Balasus, N., Jacob, D. J., Lorente, A., Maasakkers, J. D., Parker, R. J., Boesch, H., Chen, Z., Kelp, M. M., Nesser, H., and Varon, D. J.: A blended TROPOMI+GOSAT satellite data product for atmospheric methane using machine learning to correct retrieval biases, Atmospheric Measurement Techniques, 16, 3787–3807, https://doi.org/10.5194/amt-16-3787-2023, 2023.

Bao, C., Bagan, H., Te, T., Wang, Q., Boris, Z., and Kinoshita, T.: Spatiotemporal variability of methane concentrations driven by ruminant livestock in Mongolia: insights from satellite observations and machine learning, GIScience & Remote Sensing, 62, 2582118, https://doi.org/10.1080/15481603.2025.2582118, 2025.

Borsdorff, T., Martinez-Velarte, M. C., Sneep, M., ter Linden, M., and Landgraf, J.: Random Forest Classifier for Cloud Clearing of the Operational TROPOMI XCH4 Product, Remote Sensing, 16, 1208, https://doi.org/10.3390/rs16071208, 2024.

Butz, A., Hasekamp, O. P., Frankenberg, C., Vidot, J., and Aben, I.: CH4 retrievals from space-based solar backscatter measurements: Performance evaluation against simulated aerosol and cirrus loaded scenes, Journal of Geophysical Research: Atmospheres, 115, https://doi.org/10.1029/2010JD014514, 2010.

Butz, A., Guerlet, S., Hasekamp, O., Schepers, D., Galli, A., Aben, I., Frankenberg, C., Hartmann, J.-M., Tran, H., Kuze, A., Keppel-Aleks, G., Toon, G., Wunch, D., Wennberg, P., Deutscher, N., Griffith, D., Macatangay, R., Messerschmidt, J., Notholt, J., and Warneke, T.: Toward accurate CO2 and CH4 observations from GOSAT, Geophysical Research Letters, 38, https://doi.org/10.1029/2011GL047888, 2011.

Chen, J., Hu, R., Chen, L., Liao, Z., Che, L., and Li, T.: Multi-sensor integrated mapping of global XCO2 from 2015 to 2021 with a local random forest model, ISPRS Journal of Photogrammetry and Remote Sensing, 208, 107–120, https://doi.org/10.1016/j.isprsjprs.2024.01.009, 2024.

Choi, H. and Jeong, U.: Spatiotemporal Variations of Atmospheric Methane over the Korean Peninsula from Sentinel-5P/TROPOMI Observations, Korean Journal of Remote Sensing, 42, 77–90, https://doi.org/10.7780/kjrs.2026.42.1.6, 2026.

Deutscher, N. M., Griffith, D. W. T., Paton-Walsh, C., Velazco, V. A., Wennberg, P. O., Blavier, J.-F., Washenfelder, R. A., Yavin, Y., Keppel-Aleks, G., Toon, G. C., Jones, N. B., Kettlewell, G. C., Connor, B. J., Macatangay, R. C., Wunch, D., Roehl, C., and Bryant, G. W.: TCCON data from Darwin (AU), Release GGG2020.R0, https://doi.org/10.14291/tccon.ggg2020.darwin01.R0, 2023.

Dils, B., Buchwitz, M., Reuter, M., Schneising, O., Boesch, H., Parker, R., Guerlet, S., Aben, I., Blumenstock, T., Burrows, J. P., Butz, A., Deutscher, N. M., Frankenberg, C., Hase, F., Hasekamp, O. P., Heymann, J., De Mazière, M., Notholt, J., Sussmann, R., Warneke, T., Griffith, D., Sherlock, V., and Wunch, D.: The Greenhouse Gas Climate Change Initiative (GHG-CCI): comparative validation of GHG-CCI SCIAMACHY/ENVISAT and TANSO-FTS/GOSAT CO_2 and CH_4 retrieval algorithm products with measurements from the TCCON, Atmospheric Measurement Techniques, 7, 1723–1744, https://doi.org/10.5194/amt-7-1723-2014, 2014.

East, J. D., Jacob, D. J., Balasus, N., Bloom, A. A., Bruhwiler, L., Chen, Z., Kaplan, J. O., Mickley, L. J., Mooring, T. A., Penn, E., Poulter, B., Sulprizio, M. P., Worden, J. R., Yantosca, R. M., and Zhang, Z.: Interpreting the Seasonality of Atmospheric Methane, Geophysical Research Letters, 51, e2024GL108494, https://doi.org/10.1029/2024GL108494, 2024.

Fan, L., Wan, Y., and Dai, Y.: Development of a Multi-Source Satellite Fusion Method for XCH4 Product Generation in Oil and Gas Production Areas, Applied Sciences, 14, 11100, https://doi.org/10.3390/app142311100, 2024.

Global Methane Tracker 2025 – Analysis: https://www.iea.org/reports/global-methane-tracker-2025, last access: 23 April 2026.

Hase, F., Herkommer, B., Groß, J., Blumenstock, T., Kiel, M. ä., and Dohe, S.: TCCON data from Karlsruhe (DE), Release GGG2020.R2, https://doi.org/10.14291/tccon.ggg2020.karlsruhe01.R2, 2024.

Hasekamp, O., Lorente, A., Hu, H., and Butz, A.: Algorithm Theoretical Baseline Document for Sentinel-5 Precursor Methane Retrieval, n.d.

Hu, H., Landgraf, J., Detmers, R., Borsdorff, T., Aan de Brugh, J., Aben, I., Butz, A., and Hasekamp, O.: Toward Global Mapping of Methane With TROPOMI: First Results and Intersatellite Comparison to GOSAT, Geophysical Research Letters, 45, 3682–3689, https://doi.org/10.1002/2018GL077259, 2018.

Hwang, Y. and Song, J.: Recent deep learning methods for tabular data, Communications for Statistical Applications and Methods, 30, 215–226, https://doi.org/10.29220/CSAM.2023.30.2.215, 2023.

Hwang, S., Choi, H., Kang, Y., and Im, J.: Reconstructing long-term (2003–2019) global high-resolution XCO2: bridging observational gaps with machine learning, GIScience & Remote Sensing, 63, 2627042, https://doi.org/10.1080/15481603.2026.2627042, 2026.

Imasu, R., Matsunaga, T., Nakajima, M., Yoshida, Y., Shiomi, K., Morino, I., Saitoh, N., Niwa, Y., Someya, Y., Oishi, Y., Hashimoto, M., Noda, H., Hikosaka, K., Uchino, O., Maksyutov, S., Takagi, H., Ishida, H., Nakajima, T. Y., Nakajima, T., and Shi, C.: Greenhouse gases Observing SATellite 2 (GOSAT-2): mission overview, Prog Earth Planet Sci, 10, 33, https://doi.org/10.1186/s40645-023-00562-2, 2023.

Inoue, M., Morino, I., Uchino, O., Nakatsuru, T., Yoshida, Y., Yokota, T., Wunch, D., Wennberg, P. O., Roehl, C. M., Griffith, D. W. T., Velazco, V. A., Deutscher, N. M., Warneke, T., Notholt, J., Robinson, J., Sherlock, V., Hase, F., Blumenstock, T., Rettinger, M., Sussmann, R., Kyrö, E., Kivi, R., Shiomi, K., Kawakami, S., De Mazière, M., Arnold, S. G., Feist, D. G., Barrow, E. A., Barney, J., Dubey, M., Schneider, M., Iraci, L. T., Podolske, J. R., Hillyard, P. W., Machida, T., Sawa, Y., Tsuboi, K., Matsueda, H., Sweeney, C., Tans, P. P., Andrews, A. E., Biraud, S. C., Fukuyama, Y., Pittman, J. V., Kort, E. A., and Tanaka, T.: Bias corrections of GOSAT SWIR XCO_2 and XCH_4 with TCCON data and their evaluation using aircraft measurement data, Atmospheric Measurement Techniques, 9, 3491–3512, https://doi.org/10.5194/amt-9-3491-2016, 2016.

Intergovernmental Panel on Climate Change (IPCC) (Ed.): Anthropogenic and Natural Radiative Forcing, in: Climate Change 2013 – The Physical Science Basis: Working Group I Contribution to the Fifth Assessment Report of the Intergovernmental Panel on Climate Change, Cambridge University Press, Cambridge, 659–740, https://doi.org/10.1017/CBO9781107415324.018, 2014.

Iraci, L. T., Podolske, J. R., Roehl, C., Wennberg, P. O., Blavier, J.-F., Allen, N., Wunch, D., and Osterman, G. B.: TCCON data from Edwards (US), Release GGG2020.R0, https://doi.org/10.14291/tccon.ggg2020.edwards01.R0, 2022.

Jacob, D. J., Varon, D. J., Cusworth, D. H., Dennison, P. E., Frankenberg, C., Gautam, R., Guanter, L., Kelley, J., McKeever, J., Ott, L. E., Poulter, B., Qu, Z., Thorpe, A. K., Worden, J. R., and Duren, R. M.: Quantifying methane emissions from the global scale down to point sources using satellite observations of atmospheric methane, Atmospheric Chemistry and Physics, 22, 9617–9646, https://doi.org/10.5194/acp-22-9617-2022, 2022.

Janardanan, R., Maksyutov, S., Tsuruta, A., Wang, F., Tiwari, Y. K., Valsala, V., Ito, A., Yoshida, Y., Kaiser, J. W., Janssens-Maenhout, G., Arshinov, M., Sasakawa, M., Tohjima, Y., Worthy, D. E. J., Dlugokencky, E. J., Ramonet, M., Arduini, J., Lavric, J. V., Piacentino, S., Krummel, P. B., Langenfelds, R. L., Mammarella, I., and Matsunaga, T.: Country-Scale Analysis of Methane Emissions with a High-Resolution Inverse Model Using GOSAT and Surface Observations, Remote Sensing, 12, 375, https://doi.org/10.3390/rs12030375, 2020.

Jang, J., Kim, G., Sim, J., Kim, J., and Lee, Y.: Machine Learning-Based Mapping of Daily Methane Concentration in Rice Paddies Using Meteorological Data and Satellite Images: A Case of South Korea, Korean Journal of Remote Sensing, 40, 1095–1108, https://doi.org/10.7780/kjrs.2024.40.6.1.18, 2024.

Kivi, R., Heikkinen, P., and Kyrö, E.: TCCON data from Sodankylä (FI), Release GGG2020.R1, https://doi.org/10.14291/tccon.ggg2020.sodankyla01.R1, 2026.

Kuze, A., Suto, H., Nakajima, M., and Hamazaki, T.: Thermal and near infrared sensor for carbon observation Fourier-transform spectrometer on the Greenhouse Gases Observing Satellite for greenhouse gases monitoring, Appl. Opt., AO, 48, 6716–6733, https://doi.org/10.1364/AO.48.006716, 2009.

Kuze, A., Suto, H., Shiomi, K., Kawakami, S., Tanaka, M., Ueda, Y., Deguchi, A., Yoshida, J., Yamamoto, Y., Kataoka, F., Taylor, T. E., and Buijs, H. L.: Update on GOSAT TANSO-FTS performance, operations, and data products after more than 6 years in space, Atmospheric Measurement Techniques, 9, 2445–2461, https://doi.org/10.5194/amt-9-2445-2016, 2016.

Lee, D., Choi, W., Hong, H., and Lee, H.: Global Estimation of Surface Methane Using Low-Earth Orbit Satellite Data and Machine Learning: Comparison of Linear and Nonlinear Models, Korean Journal of Remote Sensing, 41, 387–400, https://doi.org/10.7780/kjrs.2025.41.2.1.12, 2025.

Li, K., Bai, K., Jiao, P., Chen, H., He, H., Shao, L., Sun, Y., Zheng, Z., Li, R., and Chang, N.-B.: Developing unbiased estimation of atmospheric methane via machine learning and multiobjective programming based on TROPOMI and GOSAT data, Remote Sensing of Environment, 304, 114039, https://doi.org/10.1016/j.rse.2024.114039, 2024.

Liu, C., Wang, W., Sun, Y., and Shan, C.: TCCON data from Hefei (PRC), Release GGG2020.R1, https://doi.org/10.14291/tccon.ggg2020.hefei01.R1, 2023.

Liu, R., Li, S., Zhang, G., Liu, M., Lu, X., Peng, S., Shen, L., Zhang, Y., Zhuang, M., Zuo, X., and Dong, J.: Recent advances in TROPOMI-based methane source detection: a systematic review, GIScience & Remote Sensing, 63, 2650822, https://doi.org/10.1080/15481603.2026.2650822, 2026.

Lorente, A., Borsdorff, T., Butz, A., Hasekamp, O., aan de Brugh, J., Schneider, A., Wu, L., Hase, F., Kivi, R., Wunch, D., Pollard, D. F., Shiomi, K., Deutscher, N. M., Velazco, V. A., Roehl, C. M., Wennberg, P. O., Warneke, T., and Landgraf, J.: Methane retrieved from TROPOMI: improvement of the data product and validation of the first 2 years of measurements, Atmospheric Measurement Techniques, 14, 665–684, https://doi.org/10.5194/amt-14-665-2021, 2021.

Maasakkers, J. D., Jacob, D. J., Sulprizio, M. P., Scarpelli, T. R., Nesser, H., Sheng, J.-X., Zhang, Y., Hersher, M., Bloom, A. A., Bowman, K. W., Worden, J. R., Janssens-Maenhout, G., and Parker, R. J.: Global distribution of methane emissions, emission trends, and OH concentrations and trends inferred from an inversion of GOSAT satellite data for 2010–2015, Atmospheric Chemistry and Physics, 19, 7859–7881, https://doi.org/10.5194/acp-19-7859-2019, 2019.

Morino, I., Velazco, V. A., Hori, A., Uchino, O., and Griffith, D. W. T.: TCCON data from Burgos, Ilocos Norte (PH), Release GGG2020.R0, https://doi.org/10.14291/tccon.ggg2020.burgos01.R0, 2022.

Morino, I., Ohyama, H., Hori, A., and Ikegami, H.: TCCON data from Rikubetsu (JP), Release GGG2020.R0, https://doi.org/10.14291/tccon.ggg2020.rikubetsu01.R0, 2022.

Morino, I., Ohyama, H., Hori, A., and Ikegami, H.: TCCON data from Tsukuba (JP), 125HR, Release GGG2020.R0, https://doi.org/10.14291/tccon.ggg2020.tsukuba02.R0, 2022.

Myhre, G., D. Shindell, F.-M. Bréon, W. Collins, J. Fuglestvedt, J. Huang, D. Koch, J.-F. Lamarque, D. Lee, B. Mendoza, T. Nakajima, A. Robock, G. Stephens, T. Takemura, and H. Zhang, 2013: Anthropogenic and natural radiative forcing. In Climate Change 2013: The Physical Science Basis. Contribution of Working Group I to the Fifth Assessment Report of the Intergovernmental Panel on Climate Change. T.F. Stocker, D. Qin, G.-K. Plattner, M. Tignor, S.K. Allen, J. Doschung, A. Nauels, Y. Xia, V. Bex, and P.M. Midgley, Eds., Cambridge University Press, pp. 659-740, doi:10.1017/CBO9781107415324.018.

Nisbet, E. G., Fisher, R. E., Lowry, D., France, J. L., Allen, G., Bakkaloglu, S., Broderick, T. J., Cain, M., Coleman, M., Fernandez, J., Forster, G., Griffiths, P. T., Iverach, C. P., Kelly, B. F. J., Manning, M. R., Nisbet-Jones, P. B. R., Pyle, J. A., Townsend-Small, A., al-Shalaan, A., Warwick, N., and Zazzeri, G.: Methane Mitigation: Methods to Reduce Emissions, on the Path to the Paris Agreement, Reviews of Geophysics, 58, e2019RG000675, https://doi.org/10.1029/2019RG000675, 2020.

Noël, S., Reuter, M., Buchwitz, M., Borchardt, J., Hilker, M., Bovensmann, H., Burrows, J. P., Di Noia, A., Suto, H., Yoshida, Y., Buschmann, M., Deutscher, N. M., Feist, D. G., Griffith, D. W. T., Hase, F., Kivi, R., Morino, I., Notholt, J., Ohyama, H., Petri, C., Podolske, J. R., Pollard, D. F., Sha, M. K., Shiomi, K., Sussmann, R., Té, Y., Velazco, V. A., and Warneke, T.: XCO2 retrieval for GOSAT and GOSAT-2 based on the FOCAL algorithm, Atmospheric Measurement Techniques, 14, 3837–3869, https://doi.org/10.5194/amt-14-3837-2021, 2021.

Notholt, J., Petri, C., Warneke, T., and Buschmann, M.: TCCON data from Bremen (DE), Release GGG2020.R1, https://doi.org/10.14291/tccon.ggg2020.bremen01.R1, 2026.

Oshio, H., Yoshida, Y., Matsunaga, T., Deutscher, N. M., Dubey, M., Griffith, D. W. T., Hase, F., Iraci, L. T., Kivi, R., Liu, C., Morino, I., Notholt, J., Oh, Y.-S., Ohyama, H., Petri, C., Pollard, D. F., Roehl, C., Shiomi, K., Sussmann, R., Té, Y., Velazco, V. A., Warneke, T., and Wunch, D.: Bias Correction of the Ratio of Total Column CH4 to CO2 Retrieved from GOSAT Spectra, Remote Sensing, 12, 3155, https://doi.org/10.3390/rs12193155, 2020.

Park, H., Lee, B., Sohn, E.-H., and Kim, J. Y.: Seasonal Variability of Solar-Induced Fluorescence and Correlation with Greenhouse Gas across Different Land Cover in East Asia, Korean Journal of Remote Sensing, 40, 579–588, https://doi.org/10.7780/kjrs.2024.40.5.1.13, 2024.

Parker, R. J., Webb, A., Boesch, H., Somkuti, P., Barrio Guillo, R., Di Noia, A., Kalaitzi, N., Anand, J. S., Bergamaschi, P., Chevallier, F., Palmer, P. I., Feng, L., Deutscher, N. M., Feist, D. G., Griffith, D. W. T., Hase, F., Kivi, R., Morino, I., Notholt, J., Oh, Y.-S., Ohyama, H., Petri, C., Pollard, D. F., Roehl, C., Sha, M. K., Shiomi, K., Strong, K., Sussmann, R., Té, Y., Velazco, V. A., Warneke, T., Wennberg, P. O., and Wunch, D.: A decade of GOSAT Proxy satellite CH_4

observations, Earth System Science Data, 12, 3383–3412, https://doi.org/10.5194/essd-12-3383-2020, 2020.

Pendergrass, D. C., Jacob, D. J., Balasus, N., Estrada, L., Varon, D. J., East, J. D., He, M., Mooring, T. A., Penn, E., Nesser, H., and Worden, J. R.: Trends and seasonality of 2019–2023 global methane emissions inferred from a localized ensemble transform Kalman filter (CHEEREIO v1.3.1) applied to TROPOMI satellite observations, Atmospheric Chemistry and Physics, 25, 14353–14369, https://doi.org/10.5194/acp-25-14353-2025, 2025.

Petri, C., Vrekoussis, M., Rousogenous, C., Warneke, T., Sciare, J., and Notholt, J.: TCCON data from Nicosia (CY), Release GGG2020.R1, https://doi.org/10.14291/tccon.ggg2020.nicosia01.R1, 2024.

Pollard, D. F., Robinson, J., and Shiona, H.: TCCON data from Lauder (NZ), Release GGG2020.R0, https://doi.org/10.14291/tccon.ggg2020.lauder03.R0, 2022.

Prather, M. J., Holmes, C. D., and Hsu, J.: Reactive greenhouse gas scenarios: Systematic exploration of uncertainties and the role of atmospheric chemistry, Geophysical Research Letters, 39, https://doi.org/10.1029/2012GL051440, 2012.

Qu, Y., Wei, J., Xing, H., Shi, X., Ao, Z., and Meng, X.: Global Estimates of Daily Gapless Atmospheric XCH4 Concentrations From Satellite and Reanalysis Data During 2003–2020, IEEE Transactions on Geoscience and Remote Sensing, 63, 1–12, https://doi.org/10.1109/TGRS.2025.3593486, 2025.

Qu, Z., Jacob, D. J., Shen, L., Lu, X., Zhang, Y., Scarpelli, T. R., Nesser, H., Sulprizio, M. P., Maasakkers, J. D., Bloom, A. A., Worden, J. R., Parker, R. J., and Delgado, A. L.: Global distribution of methane emissions: a comparative inverse analysis of observations from the TROPOMI and GOSAT satellite instruments, Atmospheric Chemistry and Physics, 21, 14159–14175, https://doi.org/10.5194/acp-21-14159-2021, 2021.

Saunois, M., Martinez, A., Poulter, B., Zhang, Z., Raymond, P. A., Regnier, P., Canadell, J. G., Jackson, R. B., Patra, P. K., Bousquet, P., Ciais, P., Dlugokencky, E. J., Lan, X., Allen, G. H., Bastviken, D., Beerling, D. J., Belikov, D. A., Blake, D. R., Castaldi, S., Crippa, M., Deemer, B. R., Dennison, F., Etiope, G., Gedney, N., Höglund-Isaksson, L., Holgerson, M. A., Hopcroft, P. O., Hugelius, G., Ito, A., Jain, A. K., Janardanan, R., Johnson, M. S., Kleinen, T., Krummel, P. B., Lauerwald, R., Li, T., Liu, X., McDonald, K. C., Melton, J. R., Mühle, J., Müller, J., Murguia-Flores, F., Niwa, Y., Noce, S., Pan, S., Parker, R. J., Peng, C., Ramonet, M., Riley, W. J., Rocher-Ros, G., Rosentreter, J. A., Sasakawa, M., Segers, A., Smith, S. J., Stanley, E. H., Thanwerdas, J., Tian, H., Tsuruta, A., Tubiello, F. N., Weber, T. S., van der Werf, G. R., Worthy, D. E. J., Xi, Y., Yoshida, Y., Zhang, W., Zheng, B., Zhu, Q., Zhu, Q., and Zhuang, Q.: Global Methane Budget 2000–2020, Earth System Science Data, 17, 1873–1958, https://doi.org/10.5194/essd-17-1873-2025, 2025.

Schneising, O., Buchwitz, M., Hachmeister, J., Vanselow, S., Reuter, M., Buschmann, M., Bovensmann, H., and Burrows, J. P.: Advances in retrieving XCH_4 and XCO from Sentinel-5 Precursor: improvements in the scientific TROPOMI/WFMD algorithm, Atmospheric Measurement Techniques, 16, 669–694, https://doi.org/10.5194/amt-16-669-2023, 2023.

Sha, M. K., Langerock, B., Blavier, J.-F. L., Blumenstock, T., Borsdorff, T., Buschmann, M., Dehn, A., De Mazière, M., Deutscher, N. M., Feist, D. G., García, O. E., Griffith, D. W. T., Grutter, M., Hannigan, J. W., Hase, F., Heikkinen, P., Hermans, C., Iraci, L. T., Jeseck, P., Jones, N., Kivi, R., Kumps, N., Landgraf, J., Lorente, A., Mahieu, E., Makarova, M. V., Mellqvist, J., Metzger, J.-M., Morino, I., Nagahama, T., Notholt, J., Ohyama, H., Ortega, I., Palm, M., Petri, C., Pollard, D. F., Rettinger, M., Robinson, J., Roche, S., Roehl, C. M., Röhling, A. N., Rousogenous, C., Schneider, M., Shiomi, K., Smale, D., Stremme, W., Strong, K., Sussmann, R., Té, Y., Uchino, O., Velazco, V. A., Vigouroux, C., Vrekoussis, M., Wang, P., Warneke, T., Wizenberg, T., Wunch, D., Yamanouchi, S., Yang, Y., and Zhou, M.: Validation of methane and carbon monoxide from Sentinel-5 Precursor using TCCON and NDACC-IRWG stations, Atmospheric Measurement Techniques, 14, 6249–6304, https://doi.org/10.5194/amt-14-6249-2021, 2021.

Shiomi, K., Kawakami, S., Ohyama, H., Arai, K., Okumura, H., Ikegami, H., and Usami, M.: TCCON data from Saga (JP), Release GGG2020.R0, https://doi.org/10.14291/tccon.ggg2020.saga01.R0, 2022.

Sussmann, R., Rettinger, M., and Mostafavi Pak, N.: TCCON data from Garmisch (DE), Release GGG2020.R1, https://doi.org/10.14291/tccon.ggg2020.garmisch01.R1, 2025.

Suto, H., Kataoka, F., Kikuchi, N., Knuteson, R. O., Butz, A., Haun, M., Buijs, H., Shiomi, K., Imai, H., and Kuze, A.: Thermal and near-infrared sensor for carbon observation Fourier transform spectrometer-2 (TANSO-FTS-2) on the Greenhouse gases Observing SATellite-2 (GOSAT-2) during its first year in orbit, Atmospheric Measurement Techniques, 14, 2013–2039, https://doi.org/10.5194/amt-14-2013-2021, 2021.

Té, Y., Jeseck, P., and Janssen, C.: TCCON data from Paris (FR), Release GGG2020.R0, https://doi.org/10.14291/tccon.ggg2020.paris01.R0, 2022.

Umezawa, T., Tohjima, Y., Terao, Y., Sasakawa, M., Müller, A., Saeki, T., Machida, T., Nakaoka, S.-I., Nara, H., Nomura, S., Nishihashi, M., Mukai, H., Frey, M. M., Morino, I., Ohyama, H., Yoshida, Y., Zeng, J., Noda, H., Saito, M., Matsunaga, T., Sugita, T., Tanimoto, H., Niwa, Y., Ito, A., Yamashita, Y., Shirai, T., Ishizawa, M., Ishijima, K., Tsuboi, K., Sawa, Y., and Matsueda, H.: Long-term and interannual variations of atmospheric methane observed by the NIES and collaborative observation networks, Prog Earth Planet Sci, 12, 39, https://doi.org/10.1186/s40645-025-00711-9, 2025.

Veefkind, J. P., Aben, I., McMullan, K., Förster, H., de Vries, J., Otter, G., Claas, J., Eskes, H. J., de Haan, J. F., Kleipool, Q., van Weele, M., Hasekamp, O., Hoogeveen, R., Landgraf, J., Snel, R., Tol, P., Ingmann, P., Voors, R., Kruizinga, B., Vink, R., Visser, H., and Levelt, P. F.: TROPOMI on the ESA Sentinel-5 Precursor: A GMES mission for global observations of the atmospheric composition for climate, air quality and ozone layer applications, Remote Sensing of Environment, 120, 70–83, https://doi.org/10.1016/j.rse.2011.09.027, 2012.

Wang, W., He, J., Feng, H., and Jin, Z.: High-Coverage Reconstruction of XCO2 Using Multisource Satellite Remote Sensing Data in Beijing–Tianjin–Hebei Region, International Journal of Environmental Research and Public Health, 19, 10853, https://doi.org/10.3390/ijerph191710853, 2022.

Wang, F., Maksyutov, S., Janardanan, R., Ito, A., Morino, I., Yoshida, Y., Someya, Y., Tohjima, Y., Kelly, B. F. J., Kaiser, J. W., Lan, X., Mammarella, I., and Matsunaga, T.: Methane emissions from Australia estimated by inverse analysis using in-situ and Satellite (GOSAT) atmospheric observations, GIScience & Remote Sensing, 62, 2488595, https://doi.org/10.1080/15481603.2025.2488595, 2025.

Warneke, T., Petri, C., Notholt, J., and Buschmann, M.: TCCON data from Orléans (FR), Release GGG2020.R1, https://doi.org/10.14291/tccon.ggg2020.orleans01.R1, 2024.

Wennberg, P. O., Roehl, C. M., Wunch, D., Toon, G. C., Blavier, J.-F., Washenfelder, R., Keppel-Aleks, G., and Allen, N. T.: TCCON data from Park Falls (US), Release GGG2020.R1, https://doi.org/10.14291/tccon.ggg2020.parkfalls01.R1, 2022.

Wennberg, P. O., Roehl, C. M., Wunch, D., Blavier, J.-F., Toon, G. C., Allen, N. T., Treffers, R., and Laughner, J.: TCCON data from Caltech (US), Release GGG2020.R0, https://doi.org/10.14291/tccon.ggg2020.pasadena01.R0, 2022.

Wennberg, P. O., Wunch, D., Roehl, C. M., Blavier, J.-F., Toon, G. C., and Allen, N. T.: TCCON data from Lamont (US), Release GGG2020.R1, https://doi.org/10.14291/tccon.ggg2020.lamont01.R1, 2025.

Worden, J. R., Cusworth, D. H., Qu, Z., Yin, Y., Zhang, Y., Bloom, A. A., Ma, S., Byrne, B. K., Scarpelli, T., Maasakkers, J. D., Crisp, D., Duren, R., and Jacob, D. J.: The 2019 methane budget and uncertainties at 1° resolution and each country through Bayesian integration Of GOSAT total column methane data and a priori inventory estimates, Atmospheric Chemistry and Physics, 22, 6811–6841, https://doi.org/10.5194/acp-22-6811-2022, 2022.

World Energy Outlook 2022 – Analysis: https://www.iea.org/reports/world-energy-outlook-2022, last access: 23 April 2026.

Wunch, D., Toon, G. C., Blavier, J.-F. L., Washenfelder, R. A., Notholt, J., Connor, B. J., Griffith, D. W. T., Sherlock, V., and Wennberg, P. O.: The Total Carbon Column Observing Network, Philos Trans A Math Phys Eng Sci, 369, 2087–2112, https://doi.org/10.1098/rsta.2010.0240, 2011.

Wunch, D., Mendonca, J., Colebatch, O., Allen, N. T., Blavier, J.-F., Kunz, K., Roche, S., Hedelius, J., Neufeld, G., Springett, S., Worthy, D., Kessler, R., and Strong, K.: TCCON data from East Trout Lake, SK (CA), Release GGG2020.R0, https://doi.org/10.14291/tccon.ggg2020.easttroutlake01.R0, 2022.

Yoshida, Y., Ota, Y., Eguchi, N., Kikuchi, N., Nobuta, K., Tran, H., Morino, I., and Yokota, T.: Retrieval algorithm for CO_2 and CH_4 column abundances from short-wavelength infrared spectral observations by the Greenhouse gases observing satellite, Atmospheric Measurement Techniques, 4, 717–734, https://doi.org/10.5194/amt-4-717-2011, 2011.

Yoshida, Y., Someya, Y., Ohyama, H., Morino, I., Matsunaga, T., Deutscher, N. M., Griffith, D. W. T., Hase, F., Iraci, L. T., Kivi, R., Notholt, J., Pollard, D. F., Té, Y., Velazco, V. A., and Wunch, D.: Quality Evaluation of the Column-Averaged Dry Air Mole Fractions of Carbon Dioxide and Methane Observed by GOSAT and GOSAT-2, Sola, 19, 173–184, https://doi.org/10.2151/sola.2023-023, 2023.

Zhang, Y., Gautam, R., Pandey, S., Omara, M., Maasakkers, J. D., Sadavarte, P., Lyon, D., Nesser, H., Sulprizio, M. P., Varon, D. J., Zhang, R., Houweling, S., Zavala-Araiza, D., Alvarez, R. A., Lorente, A., Hamburg, S. P., Aben, I., and Jacob, D.

J.: Quantifying methane emissions from the largest oil-producing basin in the United States from space, Science Advances, 6, eaaz5120, https://doi.org/10.1126/sciadv.aaz5120, 2020.

Zhou, M., Dils, B., Wang, P., Detmers, R., Yoshida, Y., O’Dell, C. W., Feist, D. G., Velazco, V. A., Schneider, M., and De Mazière, M.: Validation of TANSO-FTS/GOSAT XCO_2 and XCH_4 glint mode retrievals using TCCON data from near-ocean sites, Atmospheric Measurement Techniques, 9, 1415–1430, https://doi.org/10.5194/amt-9-1415-2016, 2016.

Zhou, M., Wang, P., Kumps, N., Hermans, C., & Nan, W. (2022). TCCON data from Xianghe, China, Release GGG2020.R0 (Version R0) [Data set]. CaltechDATA. https://doi.org/10.14291/tccon.ggg2020.xianghe01.R0